Geophys. J. Int. (1996) **125**, 397–414

Microstructural development during nucleation and growth

Michael R. Riedel[1] and Shun-ichiro Karato[2]

[1] *Projectgroup Thermodynamics, University Potsdam, Telegrafenberg* C7, D-14473 *Potsdam, Germany*
[2] *University of Minnesota, Department of Geology and Geophysics,* 310 *Pillsbury Drive SE, Minneapolis,* MN 55455, *USA*

Accepted 1995 December 2. Received 1995 May 22; in original form 1994 July 26

SUMMARY

The microstructural development during nucleation and growth processes is studied numerically. Most of the studies are for the simple case of constant nucleation and growth rates, but a brief discussion is made of the effect of time-dependent nucleation and growth. A 3-D code is used which accounts for not only the nucleation and growth of individual new grains, but also the effects of grain impingement, and which allows for the study of both homogeneous and heterogeneous nucleation.

The microstructures are characterized by the grain-size distribution (GSD) and the cluster-size distribution (CSD). In the case of homogeneous nucleation, the development of GSD and CSD can be scaled using the Avrami time τ_{Av} and Avrami length δ_{Av}, which are related to the nucleation and growth rates. Both scaling constants have a simple physical meaning: the average grain size after the completion of the phase transformation is given by δ_{Av}, and the transformation half-time is approximately equal to τ_{Av}. The formation of a continuous chain of new-phase grains (percolation transition) is observed at ~ 30 per cent transformation degree, and the geometry of the largest cluster near the percolation threshold has fractal characteristics with a fractal dimension of ~ 2.5. The presence of preferred sites of nucleation (heterogeneous nucleation), such as grain boundaries, significantly modifies the microstructures when the spacing of nucleation sites is much larger than the Avrami length, the main effects being a reduced percolation threshold and an elongate grain shape. Some applications to the olivine–spinel transformation in subducting slabs and to the crystallization in a hypothetical magma ocean are discussed.

Key words: deep focus earthquakes, fractals, phase transitions, rheology, subduction.

1 INTRODUCTION

Various first-order phase transformations play a crucial role in the dynamics and evolution of the Earth. They include phase transformations in subducting slabs, and crystallization in a hypothetical magma ocean. Understanding the microstructural development during a first-order phase transformation is important because the effects of a phase transformation on several physical processes depend critically on microstructures. For example, the effects of a phase transformation on rheological properties are determined largely by the degree of grain-size reduction and the connectivity of fine-grained new phases (Rubie 1984; Kirby 1985). The processes of fractional crystallization and the formation of chemical stratification depend on the size of crystallized grains and their spatial connectivity (Tonks & Melosh 1990; Abe 1993).

Although some of the microstructural developments can be investigated through laboratory studies, application of laboratory results to Earth processes is not straightforward because the time scales of the two situations differ significantly. Thus a theoretical understanding of the basic physics, particularly of the time and spatial scaling laws, is critical in this area.

In order to describe the overall transition, the recombination of nucleation and growth is accomplished by a statistical model originally formulated by Johnson & Mehl (1939), Avrami (1939, 1940, 1941) and Kolmogorov (1937) and afterwards often termed the JMAK model. The assumptions of the model are as follows. At initial time, infinitesimally small nuclei of the stable phase are randomly produced at a constant rate I^V per unit volume throughout the metastable matrix. Once formed, the nuclei grow isotropically with a constant interphase boundary velocity (growth velocity) Y until growth is impeded by impingement with neighbouring growing nuclei, at which point growth at the impinged interface ceases. The process finally terminates when all the new grains are completely surrounded by other product phase grains. Later refinements of the model take into account the presence of preferred nucleation sites within the metastable starting phase (Cahn 1956) as well as a possible time evolution of the nucleation and growth rates (Kirkpatrick 1976). Both extensions are

important because they introduce the effects of heterogeneity in space and time into the JMAK model.

In the present paper, we first formulate a system of ordinary differential equations that describes nucleation and growth processes under time-varying P, T conditions on a mesoscopic scale. It is essentially analogous to the integral formulation of Kirkpatrick (1976), but is easier to handle in numerical calculations. We then use a 3-D computer simulation algorithm for the computation of the microstructural properties of the JMAK model. The variables used to characterize the microstructure are the number of isolated new-phase grains (with a grain-size distribution GSD) and the number of isolated new-phase aggregates, termed 'clusters' (with a cluster-size distribution CSD). Each cluster consists of several different impinged grains (at least of one single grain in each cluster).

The program code is able to account for changes in supersaturation during the transformation as well as for the presence of preferred nucleation sites, and is hence not restricted to the frequently considered case of homogeneous conditions both in space and time (Mahin, Hanson & Morris 1980; Orgzall & Lorenz 1988). It is further used to demonstrate the type of modifications to be expected with increasing degree of heterogeneity due to grain boundary nucleated reactions.

The coupling between transformation kinetics and varying P, T conditions is taken into account self-consistently, unlike in previous studies which use semi-empirical ansatz functions for nucleation and growth rates (Saetre, Hunderi & Nes 1986; Furu, Marthinsen & Nes 1990) to calculate the grain-size distributions in the JMAK model. Here, the program code is able to include any local change in the P, T conditions due to the first-order phase transformation itself. Finally we discuss some geophysical implications of the results.

2 FORMULATION OF THE MODEL

If a homogeneous reactant phase α becomes metastable due to a change in pressure or temperature, nuclei of the new (stable) phase β arise randomly both in time and space. According to the classical nucleation theory (e.g. Christian 1965), the continuity equation for the number of spherical nuclei $n(r, t)$ with radius r at time t is given by

$$\frac{\partial n(r,t)}{\partial t}+\frac{\partial}{\partial r}[Y(r,t)n(r,t)]=0. \tag{1}$$

The nucleation source term $I^{V}(t)$ enters the boundary condition for $n(r, t)$ at $r=0$ via

$$I^{V}(t)=Y(0,t)n(0,t). \tag{2}$$

Neglecting any transient stage of nucleation, the time development of $n(r, t)$ is entirely prescribed by the deterministic growth velocity Y of critical nuclei arising with mean nucleation rate I^{V} per unit volume.

The degree of transformation $x_{3\text{-D}}$ follows from the radial distribution function $n(r, t)$ by means of

$$x_{3\text{-D}}(t)=1-\exp\left(-\int_0^\infty \frac{4\pi}{3}r^3 n(r,t)\,dr\right) \tag{3}$$

(Kolmogorov 1937), and obeys, for constant Y, I^{V}, the well-known relationship

$$x_{3\text{-D}}(t)=1-\exp\left(-\frac{\pi}{3}I^{V}Y^3t^4\right). \tag{4}$$

More generally, for time-dependent nucleation and growth rates $I^{V}(t)$ and $Y(t)$, eqs (1)–(3) may be substituted by the following set of ordinary differential equations (see Appendix A):

$$\frac{d}{dt}X_{3\text{-D}}(t)=4Y(t)X_{2\text{-D}}(t), \tag{5a}$$

$$\frac{d}{dt}X_{2\text{-D}}(t)=\pi Y(t)X_{1\text{-D}}(t), \tag{5b}$$

$$\frac{d}{dt}X_{1\text{-D}}(t)=2Y(t)X_{0\text{-D}}(t), \tag{5c}$$

$$\frac{d}{dt}X_{0\text{-D}}(t)=I^{V}(t), \tag{5d}$$

where the following variables are defined in terms of the extended volume concept introduced by Avrami (1939, 1940, 1941):

$$X_{3\text{-D}}(t)\equiv\int_0^\infty \frac{4\pi}{3}r^3 n(r,t)\,dr \quad \text{total grain volume}, \tag{6a}$$

$$X_{2\text{-D}}(t)\equiv\int_0^\infty \pi r^2 n(r,t)\,dr \quad \text{total grain area}, \tag{6b}$$

$$X_{1\text{-D}}(t)\equiv\int_0^\infty 2r n(r,t)\,dr \quad \text{total grain diameter}, \tag{6c}$$

$$X_{0\text{-D}}(t)\equiv\int_0^\infty n(r,t)\,dr \quad \text{number of grains}. \tag{6d}$$

Taking into account the grain impingement in a statistically homogeneous medium, the transformed volume fraction in the real volume is given using the general relationship (see Appendix A)

$$x_{3\text{-D}}(t)=1-\exp[-X_{3\text{-D}}(t)]. \tag{7}$$

Equation set (5) is equivalent to Kirkpatrick's formula (Kirkpatrick 1976)

$$x_{3\text{-D}}(t)=1-\exp\left\{-\frac{4\pi}{3}\int_0^t I[P(t'),T(t')]\times\left(\int_{t'}^t Y[P(t''),T(t'')]\,dt''\right)^3 dt'\right\}. \tag{8}$$

This equation is derived by neglecting any transient phenomena in nucleation and for an infinitesimally small critical nucleus size; both these assumptions seem to be well satisfied in any geological or geophysical systems of interest, since the considered time- and length-scales are many orders of magnitude larger than the relevant values for the neglected microscopic processes (the time lag for reaching steady-state nucleation is typically a few seconds in liquids, and the critical nucleus size is generally in the submicron range).

It is well established that the JMAK model has an exact dimensional scaling which follows from the observation that I^{V} (dimension $L^{-3}T^{-1}$ in 3-D space) and Y (dimension LT^{-1}) permit the definition of a natural time-scale (Axe & Yamada 1986; Brandeis & Jaupart 1987)

$$\tau_{Av}=[I^{V}Y^3]^{-1/4} \tag{9}$$

and a natural length-scale

$$\delta_{Av}=[I^{V}/Y]^{-1/4}. \tag{10}$$

It follows that any function specifying the space–time (r, t)

development of the system is universal (i.e. independent of I^V and Y excepting a possible dimensional scale factor) when expressed in natural units (δ, τ) such that

$$r = \delta \times \delta_{Av} \quad \text{and} \quad t = \tau \times \tau_{Av}.$$

We will utilize these natural units throughout our numerical computations. More importantly, dimensional scaling permits us to relate the microstructure obtained under laboratory conditions to the microstructure expected under geological time-scales.

According to the classical Becker–Döring theory, the volume nucleation rate is given by

$$I^V = I_0 T \exp\left[-\frac{\Delta G^*_{hom} + \Delta G_{act}}{kT} \right] \tag{11}$$

(e.g. Christian 1965, Chapter 10), where I_0 is a constant, ΔG^*_{hom} is the activation energy for the formation of a critical nucleus, ΔG_{act} is the activation energy for diffusion at the surface of the nucleus, and kT is the thermal energy. ΔG^*_{hom} is dependent on the thermodynamic driving force $\Delta\mu$ (free-energy difference per unit volume between the different phases) via

$$\Delta G^*_{hom} = \frac{16\pi}{3} \frac{\sigma^3}{[\Delta\mu + \varepsilon]^2}, \tag{12}$$

where σ is the interfacial free energy and ε is the strain energy produced by the lattice misfit. The growth mechanism is often rate-controlled by the incorporation of the atomic units into the moving interface, yielding an interface-controlled growth rate according to

$$Y = Y_0 T \exp\left[-\frac{\Delta G_{act}}{kT} \right] \left\{ 1 - \exp\left(-\frac{\Delta\mu}{kT} \right) \right\}. \tag{13}$$

As an illustration, both functions are shown in Fig. 1 for the case of the $\alpha \rightarrow \beta$ transformation of olivine, the most abundant mineral in the upper mantle of the Earth.

In the case of grain-boundary nucleated reactions (i.e. heterogeneous nucleation) at a nucleation rate I^B (dimension $L^{-2}T^{-1}$), it is useful to consider, in addition to τ_{Av} and δ_{Av}, the corresponding 2-D scaling constants

$$\tau^{2\text{-D}}_{Av} = [I^B Y^2]^{-1/3} \tag{14}$$

and

$$\delta^{2\text{-D}}_{Av} = [I^B/Y]^{-1/3}, \tag{15}$$

where $(\delta^{2\text{-D}}_{Av})^2$ is the order of the mean grain area at the grain boundaries (in the sense of a 2-D cross-section), and $\tau^{2\text{-D}}_{Av}$ is approximately equal to the transformation half-time along these grain boundaries.

3 MICROSTRUCTURE SIMULATION

In order to obtain an integral solution for the time dependence of the mean grain-size and transformed volume fraction, it is sufficient to solve equation set (5) with some suitable equation expressing the time evolution of P and T, respectively (Hort & Spohn 1991; Däßler *et al.* 1993). In the constant-P, T case, of course, the well-known analytical expressions like eq. (4) apply.

While in principle it would be ideal to employ analytical solutions to predict the microstructural development, such solutions are unavailable for even the simplest constant-P, T case, with a few minor exceptions (e.g. Sekimoto 1986). Even if an approximate solution to eq. (1) could be found (e.g. Solomatov & Stevenson 1993), there still remains the unsolved problem posed by the mutual impingement of different crystals, which is itself an intrinsic stochastic problem.

Given these difficulties, computer simulation is required to close the gap between natural microstructures and those predicted by the few exact solutions to eq. (1). In order to make use of large-scale computer simulation algorithms, we have mapped the evolving microstructure onto a discrete lattice (Gawlinski & Stanley 1981). The modelled physical process corresponds to the transformation of a continuous cubic body with an 'imaginary covering mesh' of $512 \times 512 \times 512$ cells with applied periodic boundary conditions. In the homogeneous nucleation case, the nuclei are assumed to arise randomly, to be distributed with a specified density, and, once formed, to grow isotropically at a constant rate. Each nucleation event is stored by its spatial coordinates and time of origin. If a growing crystal crosses a lattice point, this point is set to the new phase β, otherwise the point remains unchanged (as phase α); the simulation principle is depicted in Fig. 2. The microstructures obtained are stored as 16 megabyte image files and are subsequently analysed, using a local selection algorithm for the determination of the 3-D cluster-size distribution (Stauffer 1981). A possible time evolution caused by changes in supersaturation, produced in turn by changes in P and T, is taken into account by means of a fourth-order Runge–Kutta solution of the ordinary differential equation system (5). The accuracy of the obtained solutions is checked (1) by reducing the cube length from 512 to 32 cells, and (2) by comparing the solution with known analytical sum rules, for example eq. (4).

A typical sequence of the generated microstructures on 2-D sections of the cube during the nucleation and growth process is shown in Fig. 3. The characteristic features of Johnson–Mehl type microstructures (Mahin *et al.* 1980) are observed; i.e., the surface of contact separating two grains nucleated at times t_1 and t_2 with $t_1 < t_2$ is a hyperboloid of revolution that is symmetric about a line joining the two nucleation sites and is convex towards the grain formed first. As a consequence, two-sided or one-sided grains ('caps') can appear in 2-D sections, the latter being due to truncated hyperboloid noses. Since the boundary between two grains is always convex towards the grain nucleated first, it is possible to establish the relative chronological sequence of the grains appearing in a 2-D section.

The CSD, contrary to the GSD, does not distinguish between different grains, since it counts impinged crystals as a single cluster. It is therefore a measure of impingement or, in terms of solidifying multicomponent melts (Brandeis, Jaupart & Allègre 1984; Spohn, Hort & Fischer 1988), of the connectivity of a growing polycrystalline network in a magma chamber.

The grain and cluster sizes are represented as the radius $\langle R \rangle$ of a sphere of equivalent volume, i.e. by

$$\text{volume} \cong \frac{4\pi}{3} \langle R \rangle^3. \tag{16}$$

Owing to our special simulation algorithm (i.e. the mapping of a continuous process onto a discrete lattice), the spatial resolution is limited by the spacing between two grid points, which is referred to as 1 *g.s.* (grid spacing) throughout this paper. The calculated GSDs and CSDs are hence of limited accuracy at small $\langle R \rangle$. In these cases, we either avoid the uncertain data or attempt to smooth them by using a spline fit.

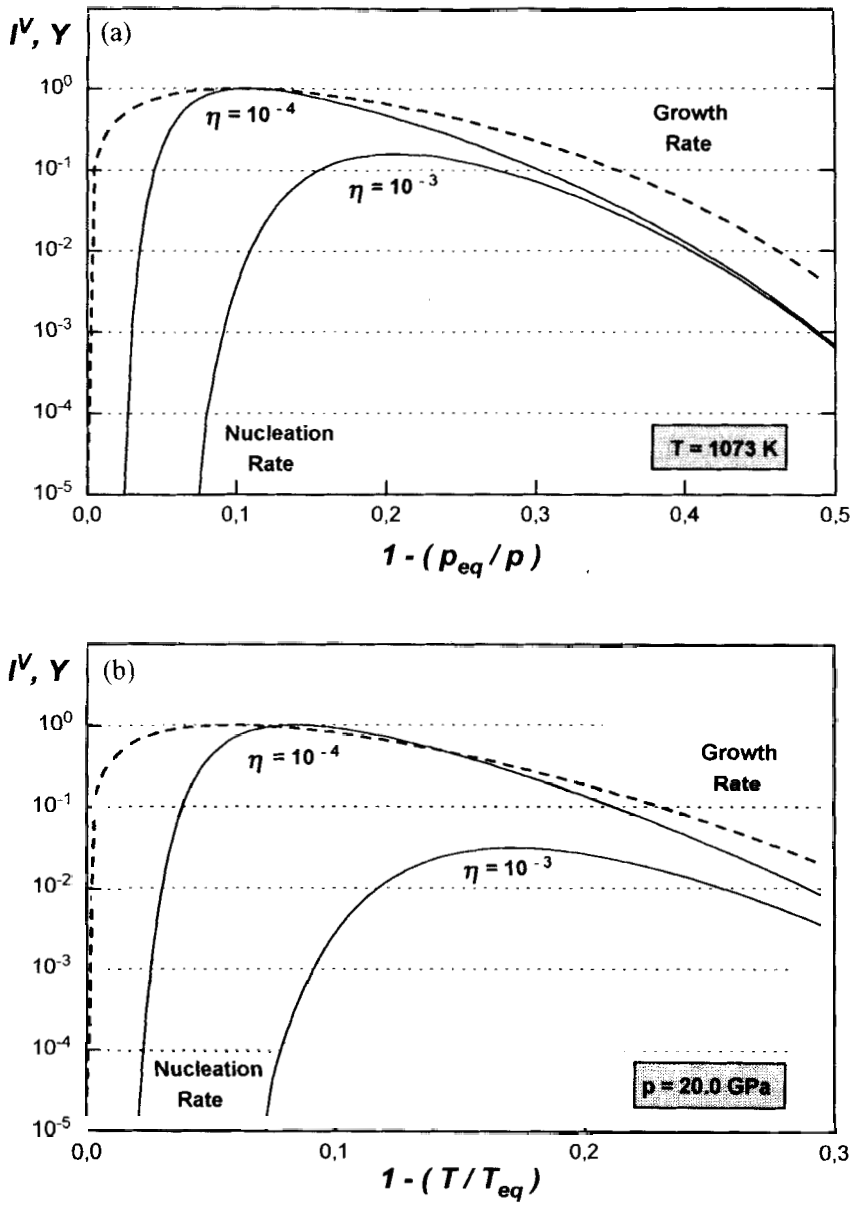

Figure 1. Dimensionless nucleation rate I^V and growth rate Y for the olivine → spinel transformation in the mantle transition zone: (a) as a function of excess pressure at $T = 1073$ K; and (b) as a function of undercooling at $P = 20.0$ GPa, for shape factors η of 10^{-3} and 10^{-4}. The growth rate is normalized by its maximum value and the nucleation rates by the maximum value for the shape factor $\eta = 10^{-4}$ (see Section 5). P_{eq} and T_{eq} are the equilibrium pressure and temperature, respectively. The chosen kinetic data set is given in Table 2.

4 CONSTANT NUCLEATION AND GROWTH RATES: JMAK MODEL

We have performed 3-D computer simulations for several parameter sets. All of them show the same generic behaviour, which can be characterized in terms of τ_{Av} and δ_{Av}. The integral transformation behaviour is depicted in Fig. 4(a) for $0 \leq t \leq \tau_{Av}$. It is seen that even at the rather low transformation level of $x_{3\text{-}D} \simeq 2.5$ per cent the total number of clusters starts to deviate from the total grain number, indicating the onset of impingement to a measurable extent.

In order to obtain a quantitative measure for the degree of impingement, Markworth (1984) introduced (under the simplifying assumption of only one homogeneous nucleation event at $t = 0$) the parameter $X_d \equiv -(1 - x_{3\text{-}D})^8 \ln(1 - x_{3\text{-}D})$ as the net volume fraction of those grains that remain entirely discrete (i.e. isolated) at time t. This parameter reaches a maximum of about 11.75 per cent at time $t \sim 0.58\tau_{av}$, when impingement between different grains is commonly observed throughout the system, and thereafter decreases rapidly to zero. As the transformation proceeds further there is a steep rise of the maximum cluster size, reflecting the percolation of β-phase clusters. At the Avrami time $t \sim \tau_{av}$ eventually, far beyond the percolation transition, the transformed volume fraction approaches 61.5 per cent, and the total cluster number is less than 5 per cent of the total grain number.

The corresponding microstructural development is plotted in Fig. 5 (GSD) and Fig. 6 (CSD). The GSD has a rectangular shape at the beginning of the transformation, which tends to become more rounded as the transformation proceeds. The

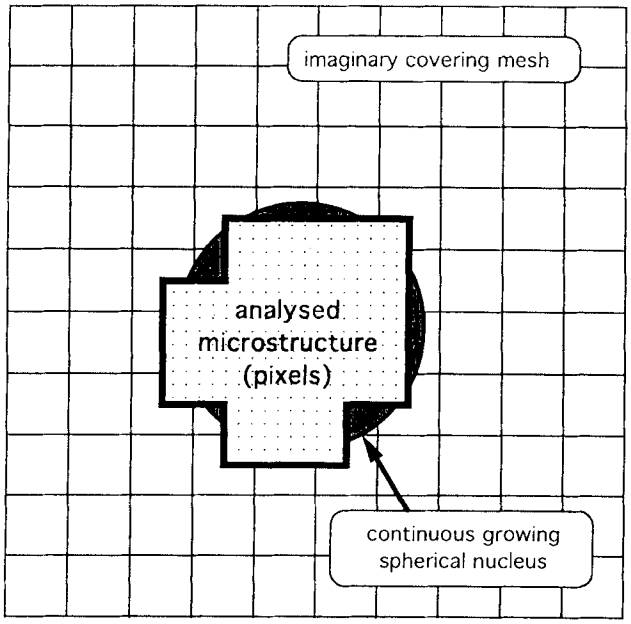

Figure 2. Illustration of the grid used by the simulation algorithm and the way in which the nucleation and growth process is mapped onto it for the computation of the grain-size and cluster-size distribution functions.

steep decrease at the large-grain-size edge is mainly a result of the assumption that the distribution of nucleation sites is homogeneous. At the small-grain-size edge, there appears to be a logarithmic increase of grain numbers during the later stages of transformation, contrary to the exponential increase frequently observed in many experiments (Randolph & Larsen 1988; Furu *et al.* 1990). The main reason for this qualitative difference seems to be the lack of any competitive grain-growth mechanism in the JMAK model. A subsequent grain growth process would significantly reduce the number of small grains and therefore flatten the small-grain-size edge of the GSD. The characteristic topological features of the JMAK microstructure (interface area, edge length, and number of faces, edges and vertices per unit volume) at completed transformation have been studied analytically by Meijering (1953). These values at $x_{3\text{-D}} = 100$ per cent are recompiled in Table 1 in terms of the Avrami length δ_{Av}.

The CSD is dominated generally by an exponentially decreasing function, after the onset of impingement at approximately 2.5 per cent transformation. There is a pronounced 'shoulder' in the distribution around the maximum grain size, as previously observed by Orgzall & Lorenz (1988). This is due to the change of the clustering type from 'compact clusters' to 'porous clusters' (Fig. 7). Clusters with a mean radius larger than the maximum grain size tend to contain increasing numbers of inclusions of α-phase, leading to an increasingly fragile network of β-phase grains with increasing mean cluster radius. The various large clusters in the system eventually become a porous β-phase framework near the percolation transition. The average cluster size $\langle S \rangle$ is given by

$$\langle S \rangle = \frac{1}{N} \sum_{s=1}^{\infty} n_s s^2 \tag{17}$$

(Stauffer & Aharony 1992), where n_s is the number of clusters containing s sites (in the imaginary covering mesh), and N is a normalization constant ($\equiv \Sigma_{s=1}^{\infty} n_s s$). At the percolation threshold, $\langle S \rangle$ apparently reaches ∞ in an infinite system (thermodynamic limit). From general percolation theory we know that at this point n_s decreases following a power law with the universal critical exponent τ:

$$n_s \sim s^{-\tau} \quad \text{for large } s \tag{18}$$

(Fisher 1967). In our simulations, the double-logarithmic plot of n_s against the size of porous clusters shows a power-law decrease with an exponent in the range of about 1.8 (Fig. 7). This is very close to the known universal value for this exponent (equal to 2.18 in 3-D space, Stauffer & Aharony 1992, p. 52), although owing to the restricted system size this value is reproduced only with limited accuracy. The compact clusters consist mainly of isolated grains, and their double-logarithmic plot changes with $x_{3\text{-D}}$ near to x_{Per} (i.e. there is no universal exponent).

Owing to the employment of an imaginary covering mesh for the microstructural analysis, a dependence of the percolation threshold value x_{Per} on the ratio between the Avrami length δ_{Av} and the basic grid-spacing unit *g.s.* is observed (Fig. 8), which transpires to be a numerical artefact of the algorithm. It is found that this threshold varies from approximately 18 per cent for $\delta_{\text{Av}} \ll g.s.$, which corresponds, owing to the grid analysis employed here, to the site percolation problem on a bcc lattice, up to 30 per cent for continuum percolation with $\delta_{\text{Av}} \gg g.s.$ (Fig. 8).

In Figs 9 and 10 we show an example of a 3-D-percolating cluster and the result of the calculation of its fractal dimension, respectively. Above the percolation threshold, the largest cluster of β-phase grains (from which the new phase framework develops) becomes increasingly compact as a result of the

Table 1. Characteristic mean quantities of the grain-size distribution in the 3-D JMAK model (after Meijering 1953). A vertex is a common point of three different interfaces.

mean grain volume	$1.116\ \delta_{Av}^3$
total interface area per unit volume	$2.479\ 1/\delta_{Av}$
total edge length per unit volume	$4.559\ 1/\delta_{Av}^2$
total number of vertices per unit volume	$5.053\ 1/\delta_{Av}^3$
average interface area of a crystal	$5.534\ \delta_{Av}^2$
average edge length of a crystal	$15.26\ \delta_{Av}$
average number of vertices of a crystal	$16\pi^2/7$
number of crystal sections per unit area (2-D section)	$\gtrsim 1.140\ 1/\delta_{Av}^2$
number of crystal boundaries per unit area (2-D section)	$\gtrsim 3.419\ 1/\delta_{Av}^2$

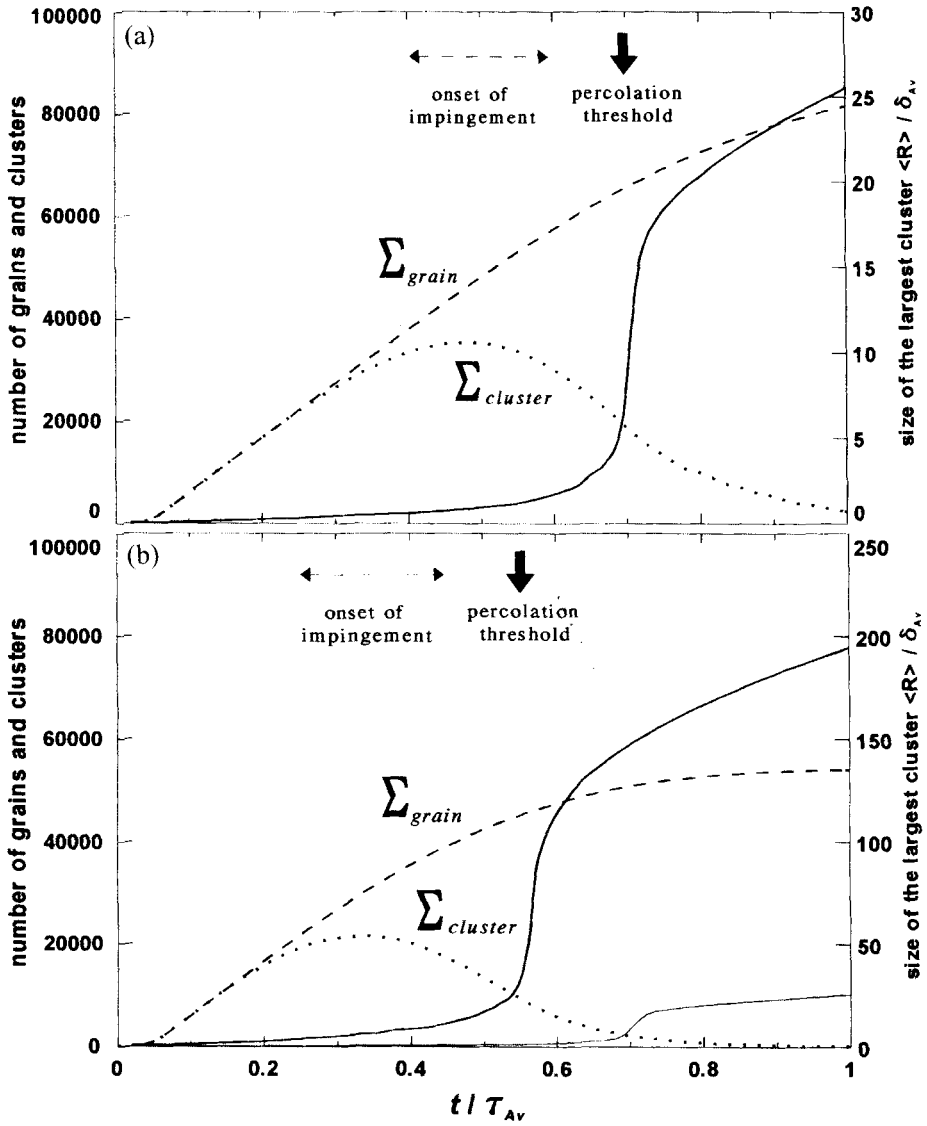

Figure 4. The scaled time dependence of the total number of grains and clusters during the phase transformation for (a) homogeneous and (b) heterogeneous nucleation, see Figs 3 and 11. The thick solid line shows the size (spherical averaged radius) of the largest cluster in the system in units of δ_{Av}. Impingement starts at a transformation degree in the range of $x_{3\text{-}D} \sim 2.5$–12.2 per cent (a) and $x_{3\text{-}D} \sim 0.35$–3.0 per cent (b). The thin solid line in (b) shows the thick line of (a) for comparism. At homogeneous nucleation, the product phase percolates at $x_{3\text{-}D} \sim 30$ per cent.

on-going phase transformation. The β-phase interconnectivity within the cluster continuously increases, while the number of α-phase inclusions decreases with $x_{3\text{-}D}$ ($> x_{Per}$). This process can be considered in the reverse direction as well. Starting from a compact β-phase polycrystal at $x_{3\text{-}D} = 100$ per cent, then, as $x_{3\text{-}D}$ decreases towards x_{Per}, the internal inclusions in the largest cluster become increasingly large, and develop a distribution in their sizes. The largest cluster at a point slightly above the percolation threshold is only homogeneous on length-scales much larger than a certain characteristic length-scale, referred to as its 'correlation length' ξ, and is rather ramified, with inclusions on all scales smaller than ξ. In fact, any percolating cluster has a *fractal* topology on scales smaller than ξ (Stauffer & Aharony 1992, p. 67). ξ is infinite at the percolation threshold x_{Per}, i.e. the largest cluster at this point is a pure fractal without internal homogeneous length-scales.

A quantitative way to study this behaviour is to determine the cluster density on different length-scales. Starting from an (arbitrary) point inside the cluster, one draws squares of increasing size L around it and calculates the mass $M(L)$ as a function of L. The result of the double-logarithmic plot of M versus L shows clearly the separation of two length-scales inside the cluster for $x_{3\text{-}D} > x_{Per}$. Whereas on a smaller length-scale $M(L)$ is a fractal with a fractal dimension of about $D \cong 2.5$ (in good agreement with the numerical results of other authors, *cf.* Stauffer & Aharony 1992; Lorenz, Orgzall & Heuer 1993), the mass distribution on a larger length-scale shows a 'regular' bulk behaviour with a constant β-phase density $\rho(L) = M(L)/L^3$. The crossover length ξ between the two internal length-scales of the largest cluster (Fig. 10) is dependent on the transformation degree $x_{3\text{-}D}$ and vanishes as $x_{3\text{-}D} \to 100$ per cent, where the largest cluster covers the whole volume.

The cluster properties just described hold for any first-order phase transition, including solid–melt transitions. It is commonly known that the change in porosity during crystallization is accompanied by a critical change in fluid permeability.

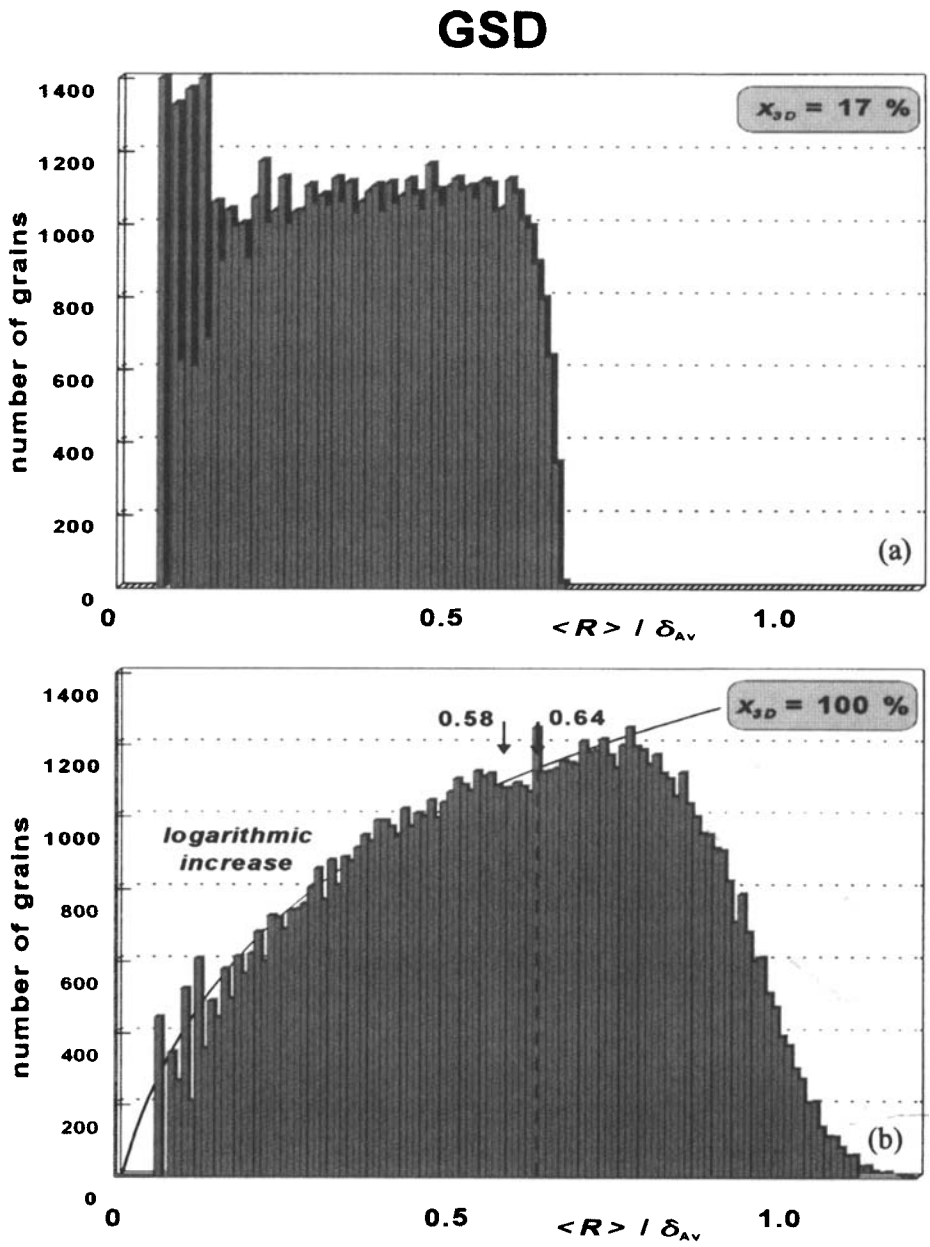

Figure 5. Grain-size distribution (GSD) for two different transformation stages (homogeneous nucleation, I^V and Y as in Fig. 3): (a) $x_{3\text{-D}} = 17$ per cent, and (b) $x_{3\text{-D}} = 100$ per cent (completed transformation). The mean grain size in (b) is given either with $0.58\delta_{Av}$ or with $0.64\delta_{Av}$, depending on the average method (with respect to the radii or to the volume distribution). The solid line shows a fit of the lower edge of the grain-size distribution to a logarithmically increasing function of the form $L\ln(1 + c\langle R\rangle/\delta_{Av})$ with $L = 512$ and $c \cong 0.128$.

Starting from the discussion presented here, we expect that, in particular, the shift of the crossover length ξ with the on-going transformation after β-phase percolation will be reflected by a systematic change in the permeability of the solid framework (*cf.* Thompson 1991).

5 HETEROGENEOUS NUCLEATION AT GRAIN BOUNDARIES

In any solid–solid phase transformation involving nucleation and growth, homogeneous nucleation is considered to be an adequate model only under idealized conditions. Heterogeneous nucleation at grain boundaries has therefore been studied as a way to avoid this limitation of the classical JMAK model (e.g. Cahn 1956). By introducing the existence of preferred nucleation sites into eq. (1), the homogeneity in space is lost, and the correction of the calculated kinetic mean values with the mean-field type equation (7) is no longer applicable. Likewise it is impossible to adopt for this problem the approach frequently taken for the study of batch crystallization (Marsh 1988; Cashman & Marsh 1988; Cashman & Ferry 1988; Buyevich & Mansurov 1990) on the basis of an exact or approximate solution for the function $n(r, t)$, often termed the crystal size distribution function, because of the unsolved impingement problem. To simplify the analysis, heterogeneous

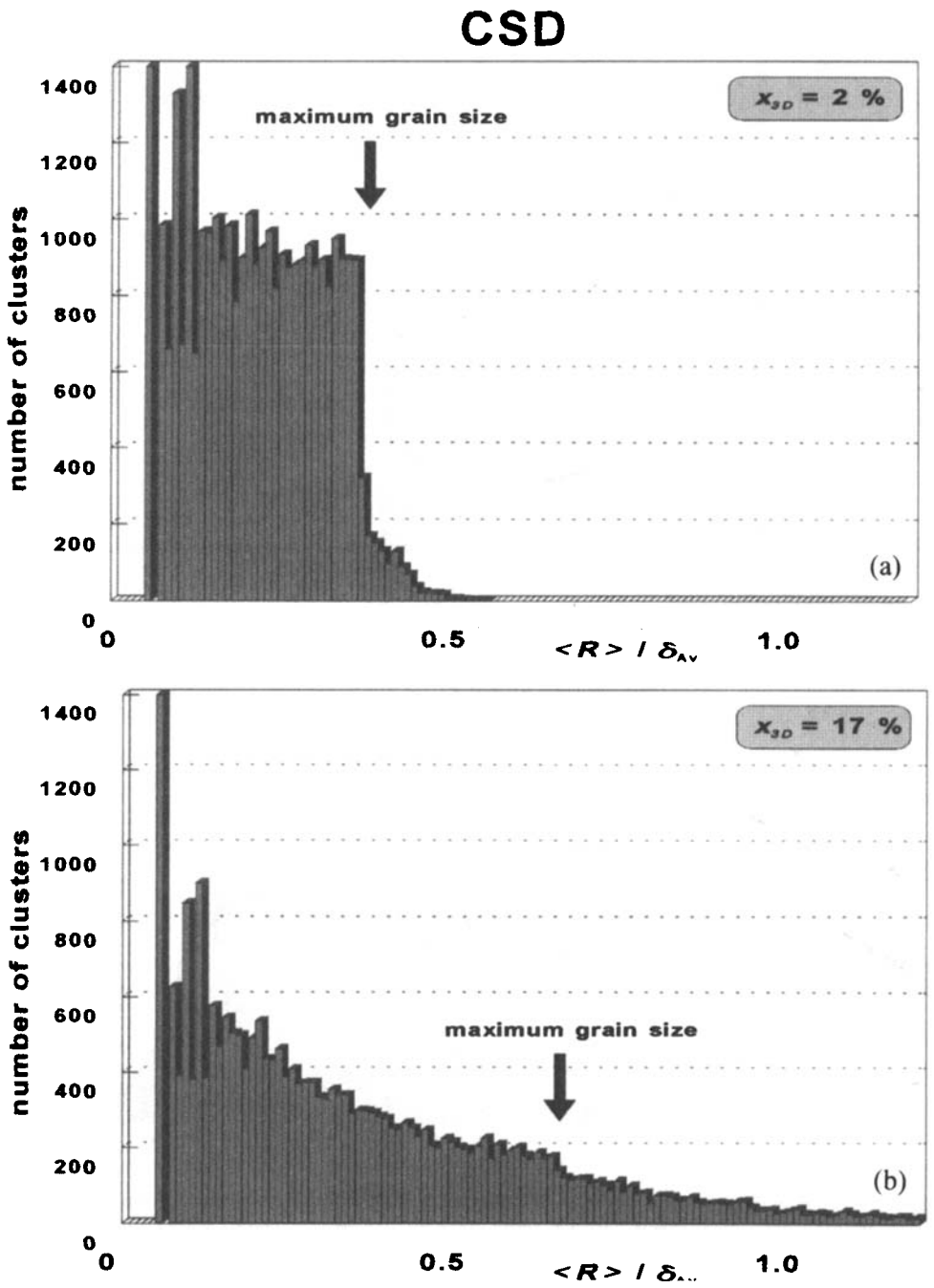

Figure 6. Cluster-size distribution (CSD) for two transformation stages (homogeneous nucleation, I^V and Y as in Fig. 3): (a) $x_{3\text{-D}} = 2$ per cent (at the beginning of impingement), and (b) $x_{3\text{-D}} = 17$ per cent.

nucleation is frequently only treated by introducing the so-called 'shape factor' η (Christian 1965) according to

$$\Delta G^*_{het} = \eta \Delta G^*_{hom}, \tag{19}$$

where ΔG^*_{het} is the activation energy for heterogeneous nucleation. η has a typical order of magnitude of 10^{-4} to 10^{-3} for solid–solid transformations, depending on the wetting angle between the two phases (Christian 1965). However, eq. (19) does not account for the spatial distribution of the nucleation sites in the host phase and is therefore not very appropriate for the study of microstructures during heterogeneous nucleation.

Instead, we again employ a 3-D simulation to circumvent this problem. To achieve this we have modified the nucleation routine in such a way that the nucleation events are now restricted to preferred grid planes, by dividing the cubic body into smaller cells with edge length L_{ini}. The corresponding grain-boundary nucleation rate I^B is then given by

$$I^B(P, T) = I^V(P, T)\, L_{ini}/3. \tag{20}$$

The initial grain size L_{ini} must be at least one order of magnitude greater than the resolution of the imaginary covering mesh in order to prevent significant (i.e. measurable) numerical errors. In all simulations we used values with $L_{ini} \gtrsim 10$ *g.s.* Owing to the presence of preferred nucleation

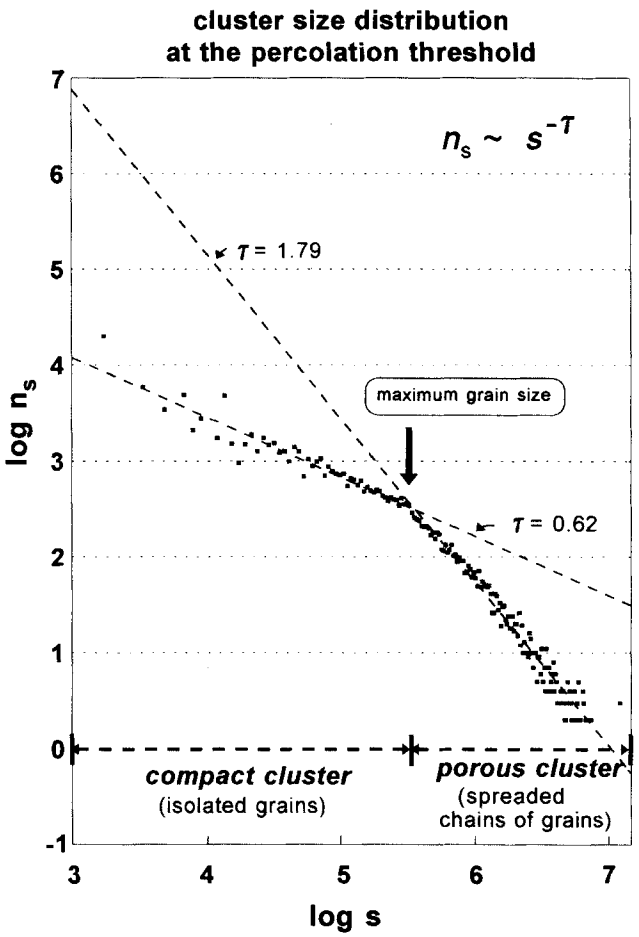

Figure 7. Double-logarithmic plot of the cluster frequency n_s consisting of s pixels (equal to the cluster volume) near to the percolation threshold (homogeneous nucleation, I^V and Y as in Fig. 3). The clusters with averaged radius larger than the maximum grain size obey approximately the generalized scaling assumption of Stauffer & Aharony (1992) with a Fisher exponent $\tau \cong 1.79$. The scatter of the data at large cluster sizes is due to the limited system size, and prevents a more precise calculation of τ (exact value is 2.18 in three dimensions according to Stauffer & Ahorony 1992). The slope at small cluster sizes (here $\tau \cong 0.62$) is not universal, i.e. it varies with $x_{3\text{-}D}$.

sites, the new length-scale L_{ini} was introduced in addition to δ_{Av}, and deviations from the generic scaling properties of the JMAK model were anticipated. It was found, however, that the microstructural properties appear to be indistinguishable from a homogeneous nucleation process if L_{ini} is lower than, or of the same order as, δ_{Av}. The reason for this is that for a homogeneous nucleation process the mean grain size in the final stages of transformation is approximately equal to δ_{Av} (see Table 1), and therefore in each pre-existing cell with edge length $L_{ini} < \delta_{Av}$ only one new phase nucleus is, on average, generated during the phase transformation. If the initial grain size L_{ini} is much larger than the Avrami length δ_{Av}, however, significant deviations from the homogeneous case occur, both with respect to the average grain size and with respect to the grain-size distribution. This is due to the mutual impingement of the grains along the preferred nucleation sites, resulting in the growth of elongated grains (Figs 11a–e). These microstructural changes are reflected by a considerable broadening of the grain-size distribution as the transformation proceeds (Fig. 12). The growth of elongate crystals causes a less steep decrease at the large-grain-size edge of the GSD, at the expense of a greater number of smaller grains, therefore reducing the number of grains with smaller sizes. The mean grain size is plotted as a function of L_{ini}/δ_{Av} at 50 per cent transition degree in Fig. 13. It can be seen that (owing to the growth of elongated grains) an increasing L_{ini}/δ_{Av}-ratio is accompanied by an increasing mean grain size. The percolation threshold is, as intuitively expected, greatly reduced by the presence of preferred nucleation sites. The critical volume fraction for percolation is reduced to as little as 40 per cent of the homogeneous case for a ratio of $L_{ini}/\delta_{Av} \cong 10$ (Fig. 14a). At the same time the transformation half-time $t_{1/2}$ is increased according to the relationship

$$t_{1/2} = \tau_{Av} \frac{\ln 2}{6} \frac{L_{ini}}{\delta_{Av}} \left\{ \int_0^1 \left[1 - \exp\left\{ -\frac{\pi}{3} \frac{L_{ini}}{\delta_{Av}} \left(\frac{t_{1/2}}{\tau_{Av}} \right)^3 \times \left[\frac{1-x^3}{3} - x^2(1-x) \right] \right\} \right] dx \right\}^{-1} \quad (21)$$

as derived by Cahn (1956).

Eq. (21) has two limiting cases:

(1) $L_{ini} \ll \delta_{Av}$ (homogeneous nucleation limit):

$$t_{1/2} = \tau_{Av} \left(\frac{3 \ln 2}{\pi} \right)^{1/4}; \quad (22)$$

(2) $L_{ini} \gg \delta_{Av}$ (elongated crystal growth dominates):

$$t_{1/2} = \tau_{Av} \frac{\ln 2}{6} \frac{L_{ini}}{\delta_{Av}}. \quad (23)$$

The simulation results show a fairly good agreement with these analytical limits (Fig. 14b).

Finally, we redraw the scaled time dependence of the total grain and cluster number for the case of a grain-boundary nucleated reaction ($L_{ini} = 10\delta_{Av}$) in Fig. 4(b). The reduction of the percolation threshold is accompanied by a much steeper increase of the percolation cluster size at this point. This is due to an amplification of the ongoing mutual impingement along the grain boundaries by the heterogeneous spatial structure of the grains in the host phase, which enhances the formation of interconnected chains of new-phase grains throughout the system volume. The larger the L_{ini}/δ_{Av}-ratio, the more pronounced this effect (similar to the effects of percolation threshold reduction and transformation half-time increase).

6 TIME-DEPENDENT NUCLEATION AND GROWTH RATES

In many geological situations, the nucleation and growth of a new phase occurs during changing P, T conditions rather than at constant P and T. The thermal and metamorphic evolution of a rock undergoing a solid–solid phase transformation in a system with time-varying supersaturation will hence be dependent on the rate laws for nucleation and growth over a certain P, T range, and the microstructural evolution is likely to reflect these P, T changes. For constant I^V and Y, all the microstructure properties are scalable by τ_{Av} and δ_{Av} as defined by eqs (9) and (10). For time-varying P, T conditions, however, this scaling is not strictly valid anymore. In order to obtain

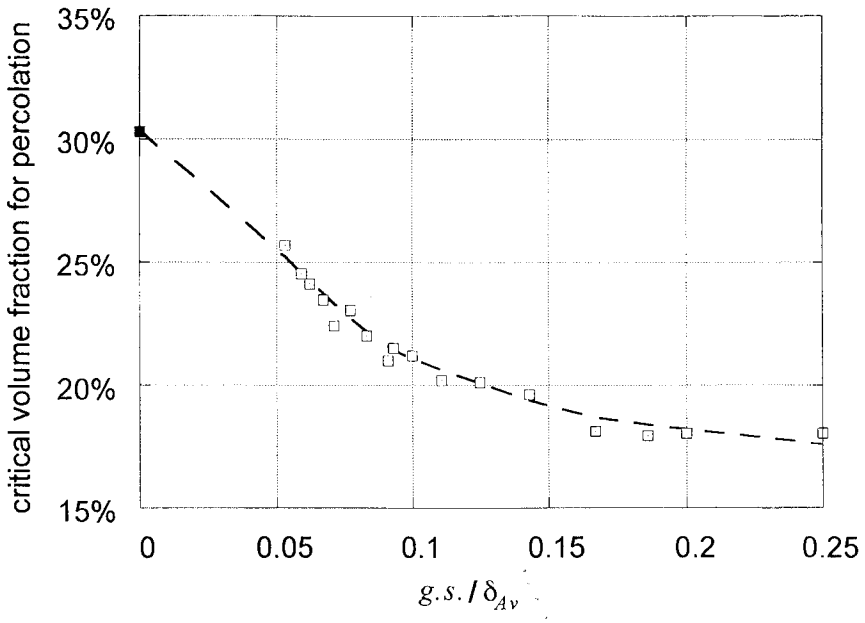

Figure 8. The dependence of the critical volume fraction for percolation (percolation threshold) during homogeneous nucleation and growth on the δ_{Av} to *g.s.* ratio (*g.s.* = grid spacing of the underlying imaginary covering mesh). The value of ~30 per cent in the continuum limit (solid square) is taken from Pike & Seager (1974).

their order of magnitude during the transformation, we calculate τ_{Av} and δ_{Av} at the beginning ($x_{3\text{-}D} = 1$ per cent) and near to the end ($x_{3\text{-}D} = 99$ per cent) of the process. It is assumed that the mean grain size of the new phase ranges between the δ_{Av} values at these two limits.

We give here a brief account of the effect of time-dependent nucleation and growth as an application of our kinetic equation set (5) to the olivine → spinel transformation in subducting slabs at around 400 km depth, based on the JMAK model with a grain-boundary nucleated reaction. There have been several experimental studies of the kinetics of this transformation (Sung 1979; Hamaya & Akimoto 1982; Rubie *et al.* 1990; Fujino & Irifune 1992), and of the equilibrium phase diagram (Katsura & Ito 1989; Akaogi, Ito & Navrotsky 1989), which together provide a rather well-constrained kinetic parameter set (Table 2). As observed previously, owing to P, T variations with time, the thermodynamic driving force $\Delta\mu$ changes during the transformation. Equation set (5) must therefore be appended with a suitable equation for $\Delta\mu(t)$. As an example, we consider the P, T profile along the coldest part of a descending slab with velocities of 4 cm yr^{-1} and of 10 cm yr^{-1}, respectively. For the sake of simplicity, we neglect the effects of the latent heat release (Däßler & Yuen 1993) and of the strain accommodation (Morris 1992) produced by the phase

Table 2. Parameter values for the $\alpha \rightarrow \beta$ transformation of Mg_2SiO_4 used in Section 6. The thermal slab model is according to McKenzie (1969).

surface energy σ	Cooper & Kohlstedt 1982	0.6 Jm^{-2}
activation energy ΔG_{act}	Rubie *et al.* 1990	4.50 x 10^5 J mol^{-1}
activation volume V_{act}	Rubie & Ross 1994	6.1 x 10^{-6} m^3 mol^{-1}
entropy difference ΔS	Akaogi *et al.* 1989	7.7 J mol^{-1} K^{-1}
volume change ΔV	Akaogi *et al.* 1989	3.16 x 10^{-6} m^3 mol^{-1}
intercept of Clapeyron equation p_0	Akaogi *et al.* 1989	11.0 GPa
molar volume of spinel	Akaogi *et al.* 1989	4.05 x 10^{-5} m^3 mol^{-1}
pre-exponential constant Y_0	Fujino & Irifune 1992 *	1.58 x 10^{12} m s^{-1} K^{-1}
pre-exponential constant I_0	Rubie & Ross 1994	1.0 x 10^{40} m^{-3} s^{-1} K^{-1}
slab length L	Turcotte & Schubert 1982	1.0 x 10^{+6} m
slab thickness D	Turcotte & Schubert 1982	8.0 x 10^{+4} m
adiabatic compressibility β_a	Turcotte & Schubert 1982	4.3 x 10^{-3} GPa^{-1}
mantle density at $z = 0$	Turcotte & Schubert 1982	3.3 x 10^{+6} g m^{-3}
Reynolds number Re for 4 cm yr^{-1}	Turcotte & Schubert 1982	42
Reynolds number Re for 10 cm yr^{-1}	Turcotte & Schubert 1982	105
lithosphere base temperature T_{base}	Turcotte & Schubert 1982	1073 K

* Fujino & Irifune observed the growth of small β-spinel aggregates along the margin of a forsterite single crystal. Taking their Fig. 2(a) with the result of the phase transformation after 20 min, we obtain as a lower limit for the spinel growth rate a value of 3.1 x 10^{-8} m s^{-1} at 15.5 GPa and 1273 K. This value is used here as a reference point for the determination of Y_0.

(a)

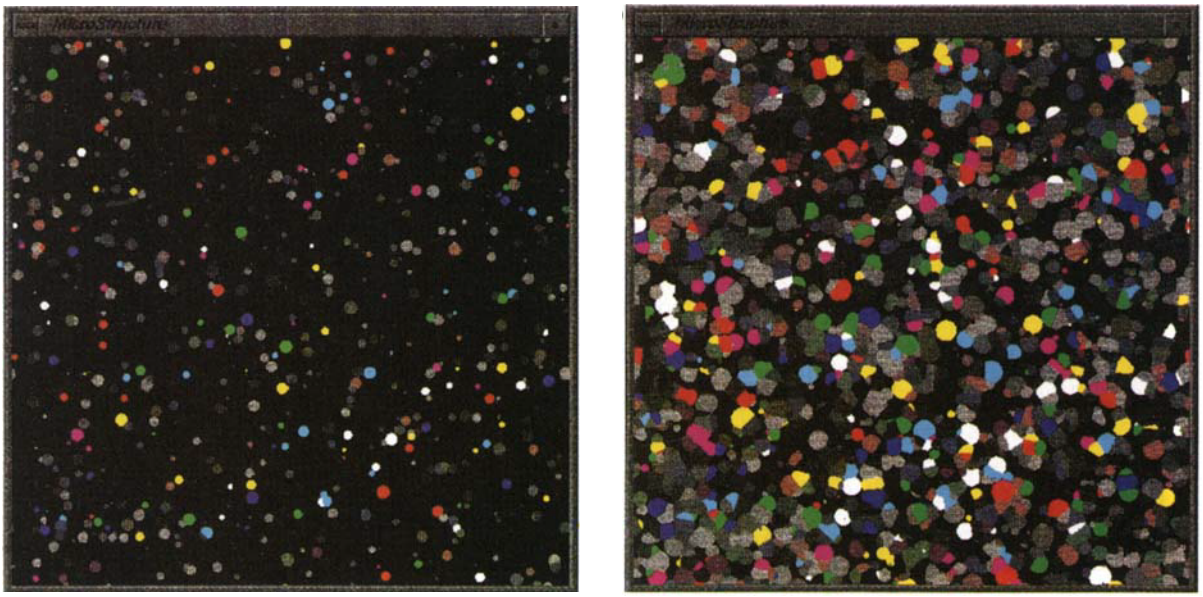

(c)

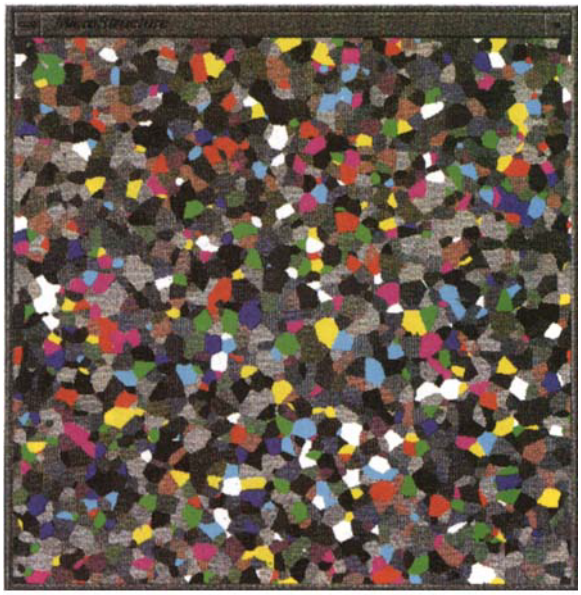

Figure 3. Snapshot pictures of the evolving 3-D nucleation and growth process using a homogeneous nucleation rate $I^V = 2000$ events per volume and time step, and a constant growth rate $Y = 0.2$ *g.s.* (grid spacing unit) per time step (equivalent to $\delta_{Av} = 10.76$ *g.s.* and $\tau_{Av} = 53.82$ steps): (a) $x_{3\text{-}D} = 10$ per cent; (b) $x_{3\text{-}D} = 50$ per cent; (c) $x_{3\text{-}D} = 100$ per cent (completed transformation). The colours are used to visualize the separated grains and have no further meaning.

(9)

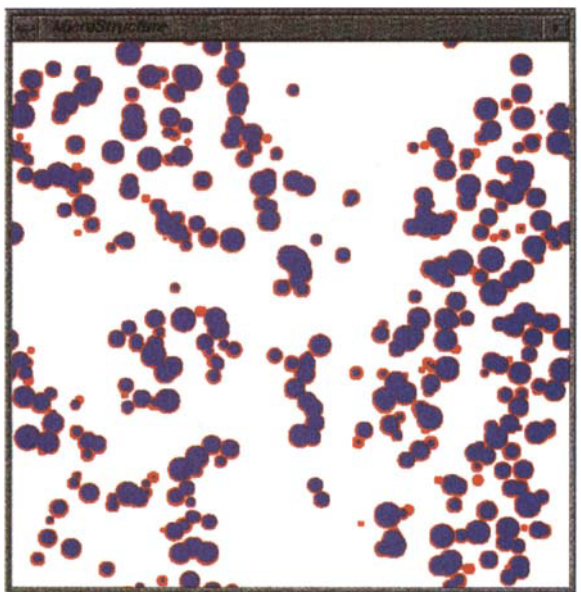

Figure 9. 2-D section of the largest cluster at the percolation threshold (parameters according to Fig. 3). All visible grains are interconnected in the third dimension and form one single large cluster (coloured blue). Its 2-D surface is shown in red. The percolation point is determined numerically as the point where the largest cluster connects all external cube sides for the first time.

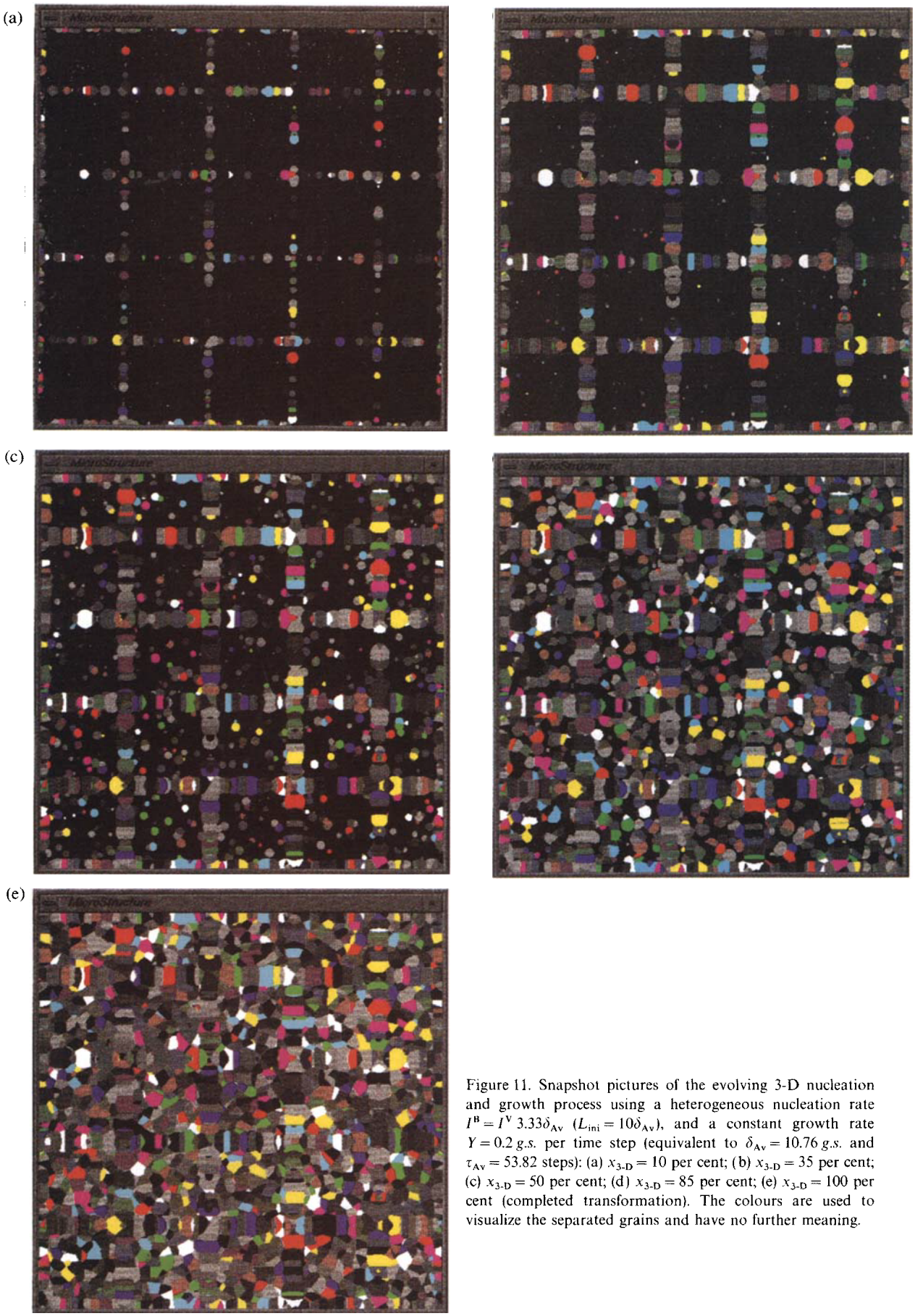

Figure 11. Snapshot pictures of the evolving 3-D nucleation and growth process using a heterogeneous nucleation rate $I^{B} = I^{V}\, 3.33\delta_{Av}$ ($L_{ini} = 10\delta_{Av}$), and a constant growth rate $Y = 0.2$ *g.s.* per time step (equivalent to $\delta_{Av} = 10.76$ *g.s.* and $\tau_{Av} = 53.82$ steps): (a) $x_{3\text{-}D} = 10$ per cent; (b) $x_{3\text{-}D} = 35$ per cent; (c) $x_{3\text{-}D} = 50$ per cent; (d) $x_{3\text{-}D} = 85$ per cent; (e) $x_{3\text{-}D} = 100$ per cent (completed transformation). The colours are used to visualize the separated grains and have no further meaning.

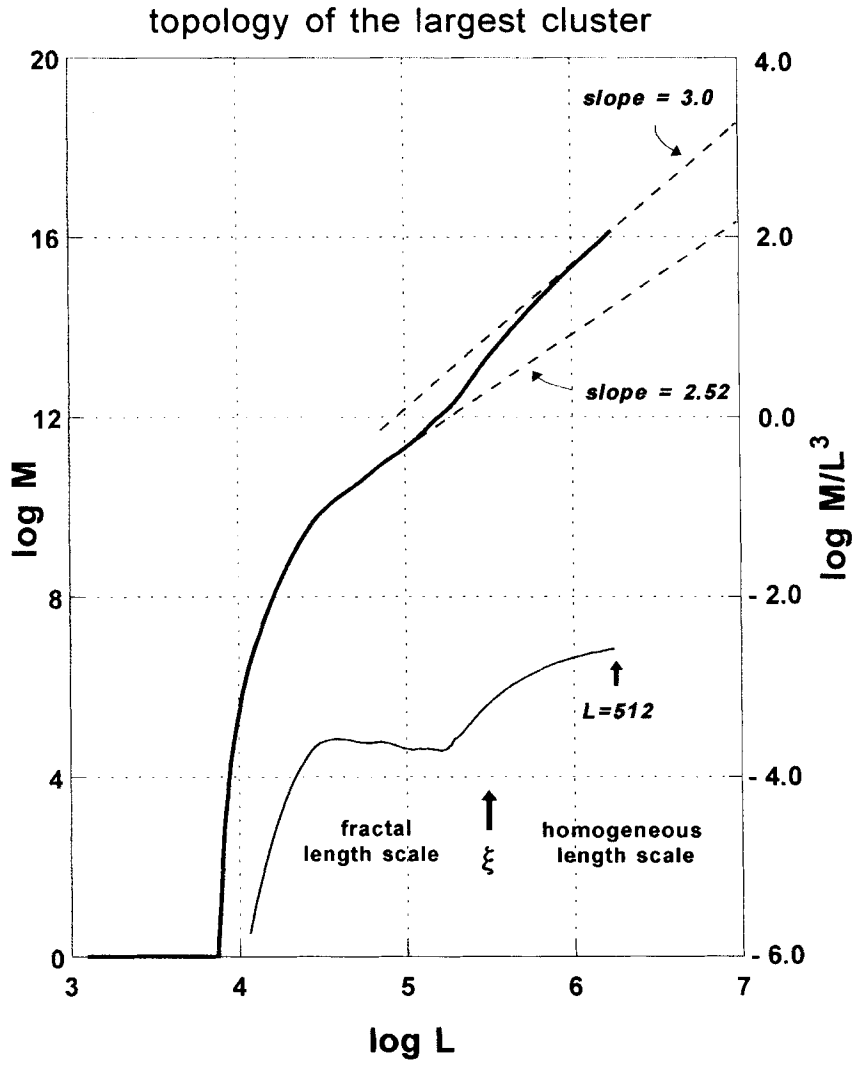

Figure 10. Calculation of the fractal dimension of the largest cluster slightly above the critical volume fraction for percolation, using the mass count method within a cube of side length L (homogeneous nucleation, I^V and Y as in Fig. 3). The thick line shows the transformed mass M (number of transformed pixels) within the cube. The thin line shows the plot of the corresponding mass density M/L^3, which is an *decreasing* function of L for a fractal object and a constant for a homogeneous bulk body. The crossover length between both length-scales of the cluster is approximately shown by ξ.

transformation, both of which provide a non-linear feedback mechanism to the P, T conditions in the slab. Given these simplifications, the pressure varies with depth z according to the mantle adiabat

$$P(t) = -\frac{1}{\beta_a} \ln\{1 - \rho_0 g \beta_a z(t)\} \tag{24}$$

(Turcotte & Schubert 1982), where β_a is the adiabatic compressibility of the mantle, ρ_0 is the mantle density at $z = 0$, and g is the acceleration of gravity. The temperature along the minima of the isotherms within the slab is given approximately by

$$T(t) = T_{base}\left\{1 - \frac{2}{\pi}\exp\left[-\frac{\pi^2 z(t)}{2LRe}\right]\right\} + T_a, \tag{25}$$

(McKenzie 1969), where L is the slab length, Re is the thermal Reynolds number, which is proportional to the descending velocity of the slab, T_{base} is the temperature at the base of the lithosphere, and T_a is a small correction term due to the adiabatic heating of the slab. The nucleation and growth rates for the olivine → spinel transition along this P, T, t path are drawn in Fig. 15(a) for the case of a subduction speed of 4 cm yr^{-1}, together with the numerically calculated degree of phase transformation. In this case the transformation is completed within a very narrow depth interval of less than 5 km near to 426 km depth, the half-time of transformation is approximately equal to the Avrami time of $\tau_{Av} \sim 50\,000$ years, and the mean grain-size is of the order of the Avrami length of $\delta_{Av} \sim 0.5$ mm (Table 3). Consequently, δ_{Av}/L_{ini} has a value of ~ 0.2, and the presence of heterogeneous nucleation sites has only minor effects on microstructures.

For a slab with a high descending velocity, for example 10 cm yr^{-1}, the transformation occurs over a much wider depth interval of up to 100 km (Fig. 15b) under entirely different P, T conditions (Table 3). The result is a much larger grain-size reduction of up to four orders in magnitude (starting from an initial olivine grain size of ~ 3 mm) in the cold slab interior. Since the scaling parameters δ_{Av} and τ_{Av} do not

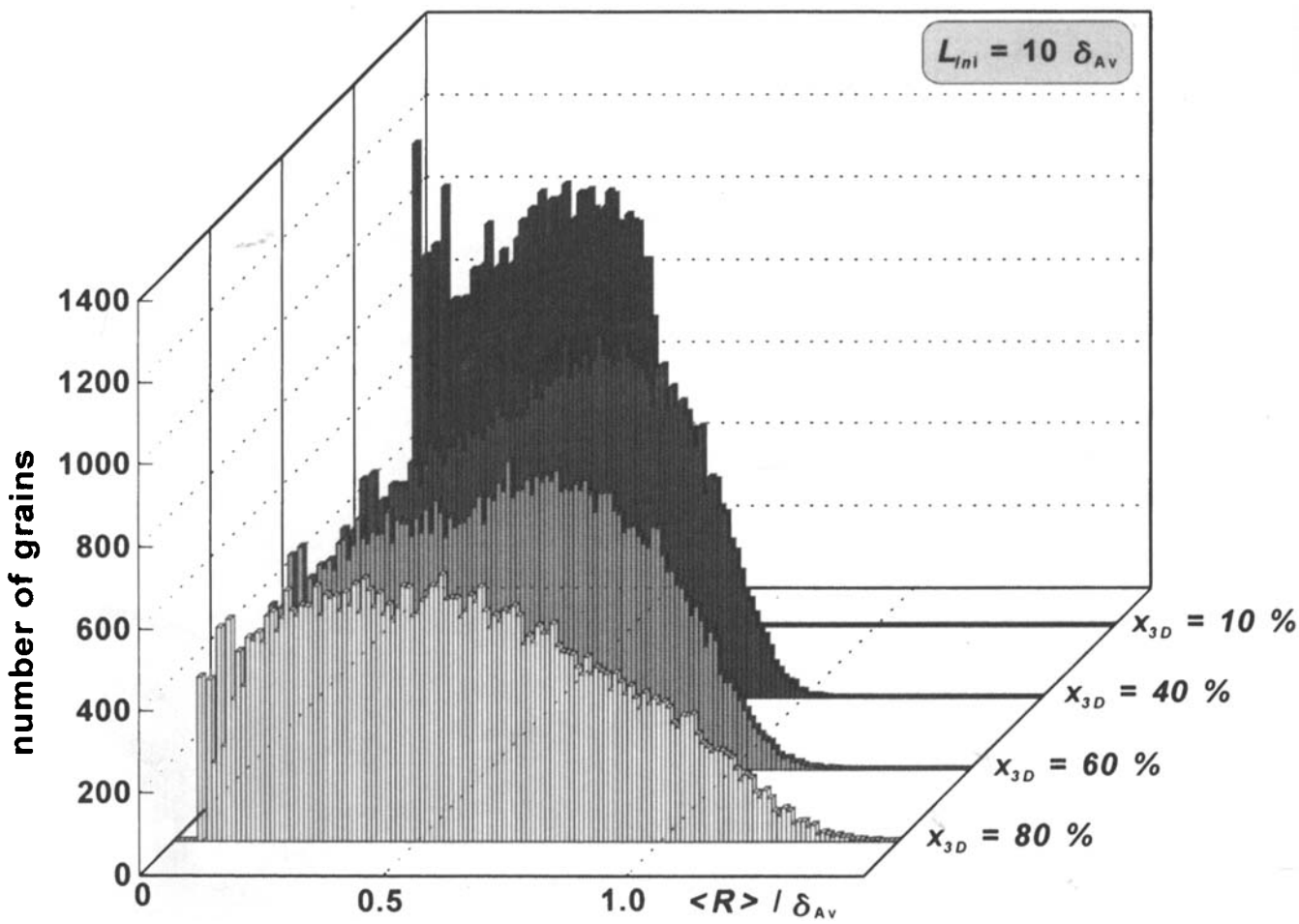

Figure 12. The evolution of the grain-size distribution (GSD) for a grain-boundary nucleated reaction (I^B and Y as in Fig. 11). The development of a large-grain-size tail to the distribution during the later stages of the transformation is due to the development of elongate grains.

Table 3. Scaling constants for the olivine → modified spinel transformation in the mantle transition zone occurring in the cool part of a subducting slab (thermodynamic data according to Table 2). The $\delta_{Av}^{2\text{-}D}$ value has a meaning only for $x_{3\text{-}D} = 1$ per cent—see text. The slab penetrates into the mantle at an angle of 45° and olivine is assumed to have an initial mean grain size of $L_{ini} = 3$ mm.

subduction velocity	4 cm yr^{-1}		10 cm yr^{-1}	
$x_{3\text{-}D}$	0.01	0.99	0.01	0.99
depth in km	424	429	551	634
p in GPa	14.16	14.33	18.55	21.47
T in K	932	935	828	866
I^V in m^{-3} s^{-1}	3.80 x 10^{-3}	1.10 x 10^{+2}	8.51 x 10^{+6}	5.01 x 10^{+7}
Y in m s^{-1}	3.78 x 10^{-16}	4.77 x 10^{-16}	3.43 x 10^{-21}	1.18 x 10^{-20}
δ_{Av} in m	5.62 x 10^{-4}	4.56 x 10^{-5}	1.41 x 10^{-7}	1.23 x 10^{-7}
$\delta_{Av}^{2\text{-}D}$ in m	4.64 x 10^{-4}	-	7.33 x 10^{-9}	-
τ_{Av} in years	4.72 x 10^{+4}	3.04 x 10^{+3}	1.31 x 10^{+6}	3.32 x 10^{+5}

change very much over this depth range, we expect that they again permit an estimate of the mean grain size and the transformation half-time. However, at initial transformation ($x_{3\text{-}D} = 1$ per cent), owing to the early impingement of the new-phase grains at the pre-existing grain boundaries, the mean grain size is further reduced by a factor

$$\delta_{Av}^{2\text{-}D}/\delta_{Av} = [3\delta_{Av}/L_{ini}]^{1/3}, \tag{26}$$

since the typical grain size at the initial stage is given in the case $\delta_{Av} \ll L_{ini}$ by $\delta_{Av}^{2\text{-}D}$ rather than by δ_{Av}, as defined by

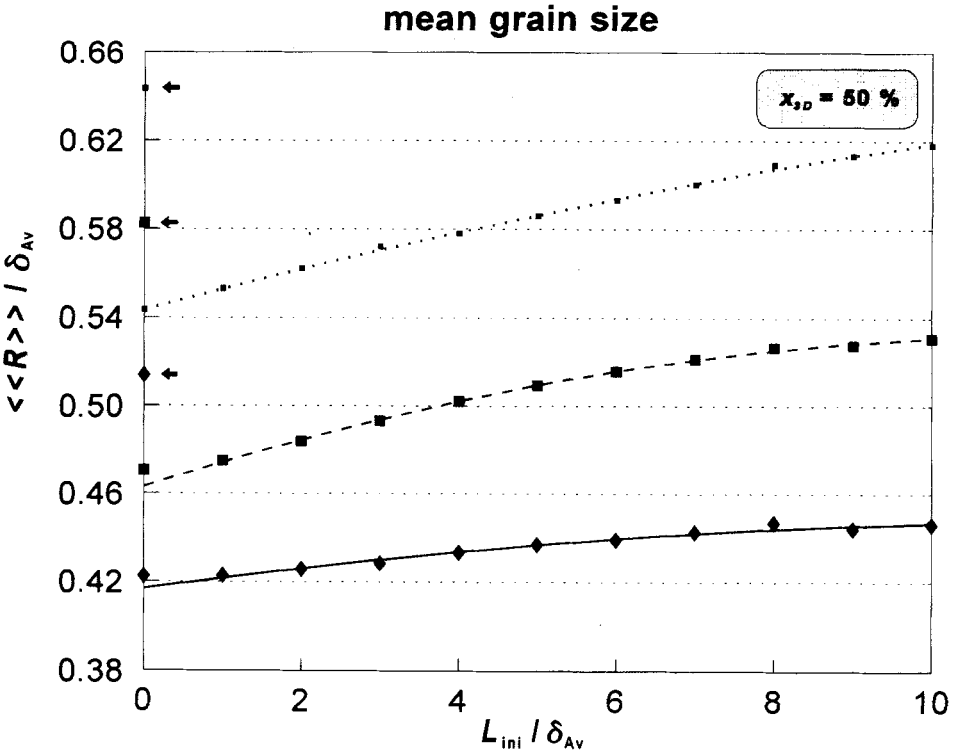

Figure 13. The dependence of the mean grain size $\langle\langle R\rangle\rangle$ on L_{ini}/δ_{Av} at 50 per cent transformation. The calculation of the mean radius is done with respect to (a) the mean grain volume (dotted line), (b) the spherical averaged GSD without empty grains (dashed line), (c) the spherical averaged GSD including all grains (solid line). The arrows on the left axis show the corresponding mean grain sizes of the JMAK model ($L_{ini} = 0$) at completed transformation ($x_{3\text{-}D} = 100$ per cent) for cases (a) to (c).

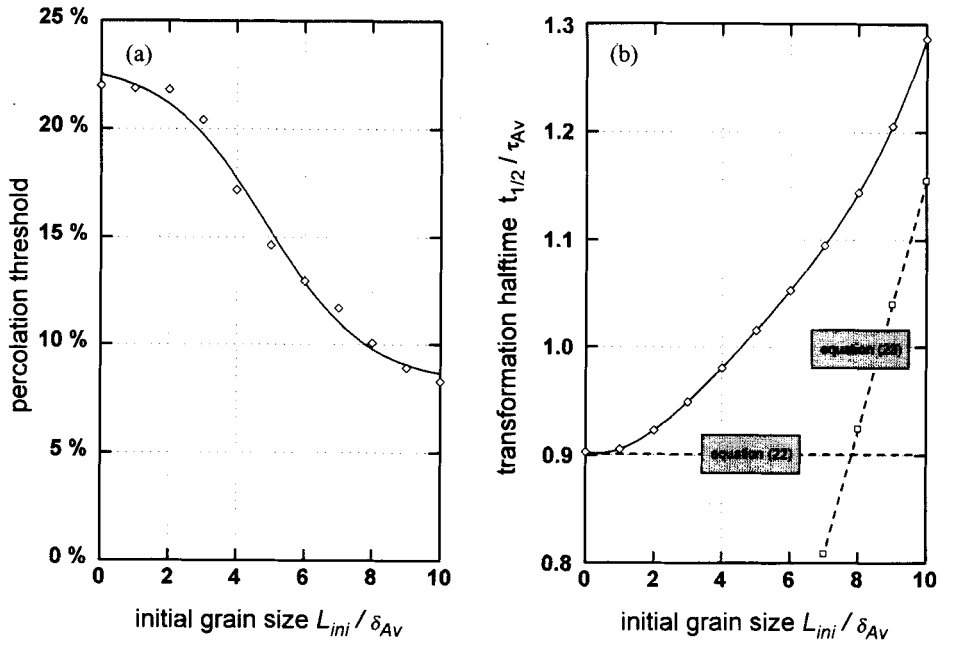

Figure 14. Dependence of the critical volume fraction for percolation (a) and the transformation half-time (b) on the degree of heterogeneity of the nucleation process (increasing number of preferred nucleation sites at grain boundaries). The two dashed lines in (b) are drawn according to the limits $L_{ini} \ll \delta_{Av}$ [homogeneous nucleation, eq. (22)] and $L_{ini} \gg \delta_{Av}$ [elongate crystal growth dominates, eq. (23)].

eq. (15). This corresponds to a further grain-size reduction of up to one order of magnitude.

In the case of a descending velocity of 4 cm yr^{-1}, we conclude that the topology of the microstructure is not much affected by possible heterogeneous nucleation at grain boundaries because $\delta_{Av} \cong L_{ini}$, where L_{ini} is typically of the order of several millimetres (Karato 1984). In contrast, $\delta_{Av} \ll L_{ini}$ for 10 cm yr^{-1}, and the observed grain-size

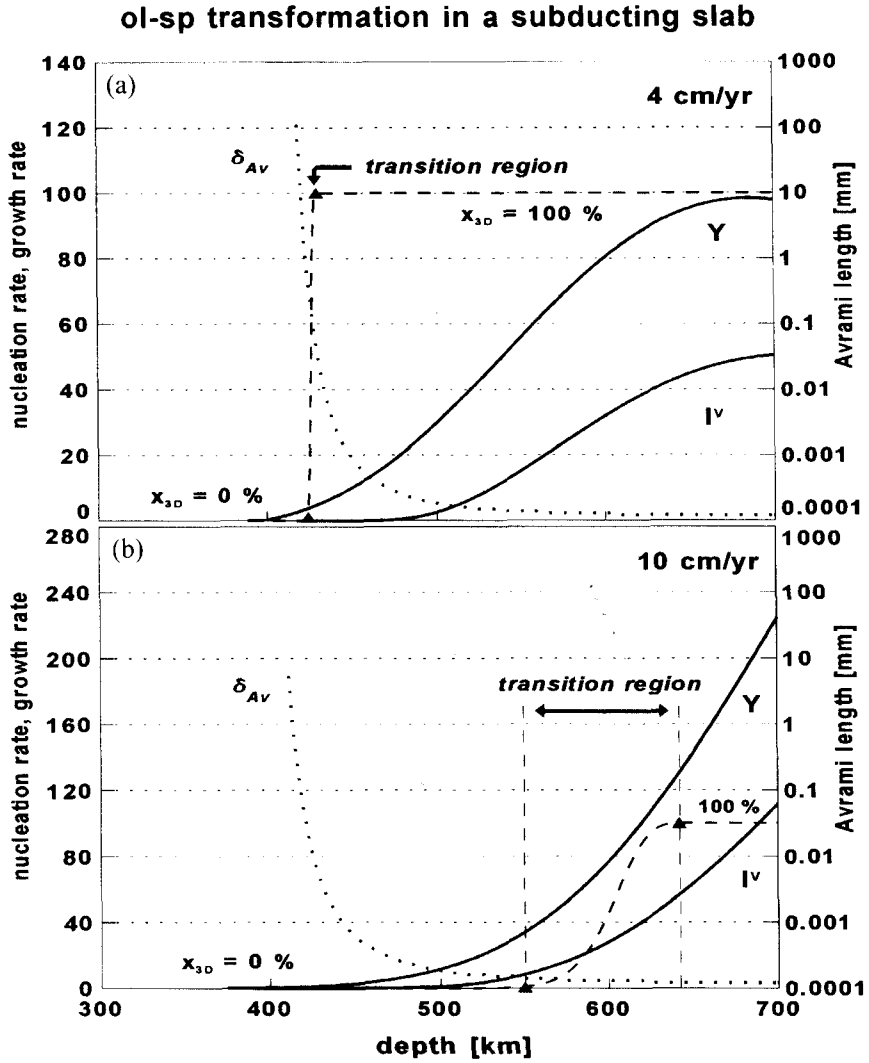

Figure 15. Nucleation rate I^V and growth rate Y along the coldest part of a descending slab with a descending velocity of (a) 4 cm yr^{-1} (units: I^V in 10^{12} m^{-3} s^{-1}, Y in 10^{-16} m s^{-1}) and (b) 10 cm yr^{-1} (units: I^V in 10^6 m^{-3} s^{-1}, Y in 10^{-22} m s^{-1}) for the olivine → spinel phase transformation (kinetic data set given in Table 2). The dotted lines shows the respective dependences of the Avrami length δ_{Av} on depth. The depth range of the phase transformation is marked with arrows, and the transition degree $x_{3\text{-}D}$ is inserted as a dashed line.

reduction leads to a significant change in microstructure (fine-grained β-phase grains formed along α-phase grain boundaries).

7 DISCUSSION

The extensions to heterogeneous nucleation (Cahn 1956) and time-dependent supersaturation (Kirkpatrick 1976) affect the scaling behaviour in different ways. In the case of grain-boundary nucleated reactions we have shown that scaling is still approximately valid for $L_{ini} \lesssim \delta_{Av}$. With increasing $L_{ini}/\delta_{Av} \gg 1$ deviations appear, one of the main effects being the drastically reduced percolation threshold visible in the CSD (Fig. 14a). When temperature and pressure change with time, both nucleation and growth rates I and Y change with time, and scaling parameters (Avrami time and length) cannot be simply used to estimate the time-scale of phase transformation nor the size of grains after a transformation. However, our numerical calculations indicate that, for the considered problem of the olivine → spinel transformation in subducting oceanic lithosphere, some rough estimates of transformation grain size (and time) after transformation can still be made using the values of δ_{Av} and τ_{Av} at an early ($x_{3\text{-}D} = 1$ per cent) and late ($x_{3\text{-}D} = 99$ per cent) stage of transformation. The reason is as follows. For a slow and warm slab, the transformation interval is very narrow (Figs 15 and 16) and the time dependence of I and Y does not play any significant role. For a fast and cold slab, on the other hand, the phase transformation occurs in a wide depth range through which both I and Y change, but the Avrami length defined locally using instantaneous I and Y does not change appreciably with time (see Figs 15 and 16). Therefore, using some *locally* defined Avrami length, it is still possible to estimate the grain size after a phase transformation.

As the result, a clear difference is seen between slow ($\lesssim$4 cm yr^{-1}) and fast ($\gtrsim$10 cm yr^{-1}) subduction: a slow slab appears to produce a relatively large spinel grain size after the transformation because the growth rate is high relative to the nucleation rate, because of the high temperature. The calculated grain size is comparable to the typical olivine grain size in an

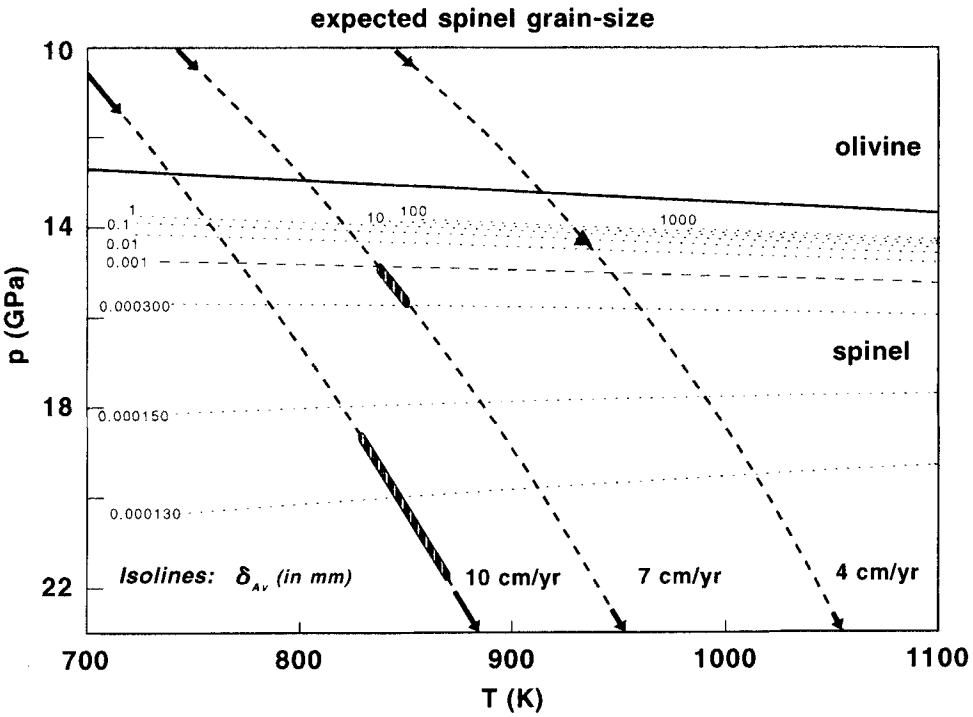

Figure 16. *P*, *T* paths in the central part of subducting slabs for slab velocities of 4, 7, and 10 cm yr^{-1} (kinetic data set given in Table 2). The hatched areas and the solid triangle mark the regions where the olivine → spinel transformation is evolving (range between $x_{3\text{-}D} = 1$ and 99 per cent). Plotted isolines for the Avrami length δ_{Av} indicate the expected mean spinel grain size. The dashed line is the isoline $\delta_{Av} = 1$ μm.

oceanic lithosphere (a few millimetres, Karato 1984). Thus we conclude that a slow slab belongs to the group of $\delta_{Av} \sim L_{ini}$, and that the role of pre-existing nucleation sites (heterogeneous nucleation) is not very important.

In fast slabs, a significantly smaller spinel grain size results from the much lower temperature at which nucleation and growth occur. The original grain size is kinetically reduced by up to four orders of magnitude by the phase transformation in the cold central portion of the slab (Table 3). Furthermore, in addition to this kinetic grain-size reduction, a topological grain-size reduction is possible as the consequence of a further nucleation mechanism. Owing to the very early impingement of the growing spinel grains along the olivine grain boundaries, elongate grain growth is likely to be accompanied by secondary nucleation at the growing interphase grain boundaries, which eventually leads to microstructures with typical grain sizes of the order of $\delta_{Av}^{2\text{-}D}$ rather than of δ_{Av}. The result would be a further grain-size reduction according to eq. (26). Hence, the role of pre-existing heterogeneities in nucleation is important for a fast slab.

We suggest that this result is directly relevant to the instability associated with the olivine → spinel transformation, which has been proposed as a trigger for deep focus earthquakes (Kirby 1987; Green & Burnley 1989; Frohlich 1994). As reported by Green & Burnley (1989), faulting occurs only in a narrow temperature interval. Furthermore, under the conditions of instability, lens-shaped regions with a crack-like morphology and containing very fine-grained spinels are found. These observations are consistent with our results, which indicate that a significant grain-size reduction is possible under the conditions of fast subduction (low temperatures).

Another example of interest is the case of a solidifying magma chamber (Kirkpatrick 1981; Lofgren 1983; Brandeis *et al.* 1984; Brandeis & Jaupart 1987). Although a crystallizing magma is a multicomponent–multiphase system and hence cannot be directly analysed with the simple JMAK model, one can find some estimate for the peak nucleation rates of several minerals precipitating from a supersaturated melt (Table 4). The inferred grain size $\delta_{Av} \sim 10^{-2}$ m appears to be in a good agreement with the observed typical grain size $\sim 10^{-3}$ m–$\sim 10^{-2}$ m in crystallized igneous rocks.

Finally, we comment briefly on the situation in a hypothetical terrestrial magma ocean. As discussed by Solomatov & Stevenson (1993), the presence of crystals has two possible consequences: fractional crystallization when the magma ocean cannot suspend crystals even at small fractions, and non-fractional crystallization when the convection is strong enough to prevent any crystal settling. The boundary between the two cases is determined mainly by the energetics of the convection, but is also dependent on further processes such as the settling velocity of crystals (which is in turn dependent on both GSD *and* CSD). The interconnectivity of the growing grains plays a crucial role with respect to the settling kinetics. A (fractal) skeleton solid will sink significantly faster than isolated (compact) grains. This is likely to result in a different mode of chemical layering at the bottom viscous boundary layer (Tonks & Melosh 1990). As we have shown, crystal impingement begins at a transformed volume fraction as low as 2.5 per cent (Fig. 4a), and crystal settling is accompanied by skeleton formation. The settling velocity, usually given in a viscous fluid by Stokes' law as proportional to the squared crystal radius, then has to be modified in a suitable way to account for the penetration of a fluid through a porous body rather than for the frictional forces of a falling sphere in a laminar flow. At the critical melt fraction $\phi_C \sim 40$ per cent, the viscosity of the partial melt rapidly increases by up to 19 orders of magnitude

Table 4. Scaling constants for a solidifying magma chamber with different melt compositions (water content) in which there is nucleation of quartz, alkaline feldspars, and plagioclase [data taken from Brandeis *et al.* (1984), p. 10 174]. The undercooling varies in the range of $\Delta T = 200$–$450\,^{\circ}C$ and was held constant during the experiments for 24 hours.

Crystal	Water content	Nucleation rate I^V in $m^{-3}\,s^{-1}$	Growth rate Y in $m\,s^{-1}$	Avrami length δ_{Av} in m	Avrami time τ_{Av} in s
Quartz	3.5 per cent	$\sim 10^{-3}$	2×10^{-11}	1.19×10^{-2}	5.95×10^{8}
	6.5 per cent	$\sim 10^{-3}$	2×10^{-11}	1.19×10^{-2}	5.95×10^{8}
	12 per cent	$\sim 10^{-3}$	10^{-10}	1.78×10^{-2}	1.78×10^{8}
Alkali feldspar	3.5 per cent	$\sim 10^{-4}$	10^{-9}	5.62×10^{-2}	5.62×10^{7}
	6.5 per cent	$\sim 10^{-3}$	10^{-10}	1.78×10^{-2}	1.78×10^{8}
	12 per cent	$\sim 10^{-3}$	3×10^{-11}	1.32×10^{-2}	4.39×10^{8}
Plagio-clase	3.5 per cent	$\sim 10^{-4}$	10^{-11}	1.78×10^{-2}	1.78×10^{9}
	6.5 per cent	$\sim 10^{-3}$	5×10^{-10}	2.66×10^{-2}	5.32×10^{7}
	12 per cent	$\sim 10^{-3}$	3×10^{-11}	1.32×10^{-2}	4.39×10^{8}

(Abe 1993). However, this kind of percolation transition takes place under entirely different conditions (vigorous convection, gravitational and buoyancy forces) and hence cannot be readily analysed by a simple nucleation and growth process, since the Avrami analysis assumes that the new-phase crystals do not move.

A serious limitation of any nucleation and growth model, particularly for the description of polymorphic solid–solid phase transformations, is the absence of the subsequent grain growth stage. This is a consequence of the lack of a grain-boundary energy term in the basic equations. However, using a numerical simulation procedure, it is easy to append a suitable algorithm for this purpose. In a large ensemble of grains of different sizes, the individual grains will grow or shrink with different velocities. As a first approximation, one replaces the individual velocity of a grain with the mean velocity of all grains of the same size R (Atkinson 1988; Ryum & Hunderi 1989). The mean velocity of a grain of size R is then given by $v_R \sim (R^{-1} - R_C^{-1})$, where $R_C(t)$ is a scaling grain size of the ongoing drift process (i.e. the with $R_C(t)$ normalized GSD does not change with time). The result is an exhaustion of smaller grains and a shift of the mean grain size towards larger values. The time-scale of this process is completely different from τ_{Av}. Contrary to the latter, it is not governed by the degree of metastability but is solely related to the surface area to volume ratio in the grain-growing polycrystal and to the mobility of atomic units in the solid phase. Typically, it is several orders of magnitude larger than τ_{Av}. Thus as a first approximation it is sensible to compute the grain-size distribution in a solid–solid transformation on the basis of a pure nucleation and growth model. The resultant GSD serves as a reference for further (slow) modifications resulting from grain growth. In this way, it should be possible to calculate the grain-size development for a realistic P, T profile in a subducting slab. The strength of a slab at greater depths will be affected by various phase transformations in the transition zone of the Earth's mantle. Grain-size reduction is likely to occur, which will lead to rheological softening of the slab. The degree of softening depends on the amount of grain-size reduction, and hence on the kinetics of nucleation and growth. Work on this particular problem is currently in progress.

ACKNOWLEDGMENTS

This research was supported by the Deutsche Forschungsgemeinschaft and the National Science Foundation, grant EAR-9206683 (to SK). Part of this work was performed during MRR's stay at the University of Minnesota and the Minnesota Supercomputer Institute in spring 1992. One author (MRR) wishes to thank Prof. D.A. Yuen (Minnesota Supercomputer Institute) for his support and continuous interest in the considered problem.

We thank D. C. Rubie and S. J. Covey-Crump for critical reviews.

REFERENCES

Abe, Y., 1993. Thermal evolution and chemical differentiation of the terrestrial magma ocean, in *Evolution of the Earth and Planets,* pp. 41–54, eds Takahashi, E., Jeanloz, R. & Rubie, D., Geophys. Monograph **74,** American Geophysical Union, Washington, DC.

Akaogi, M., Ito, E. & Navrotsky, A., 1989. Olivine-modified spinel–spinel transitions in the system Mg_2SiO_4–Fe_2SiO_4: calorimetric measurements, thermochemical calculation, and geophysical implication, *J. geophys. Res. B,* **94,** 15 671–15 685.

Atkinson, H.V., 1988. Theories of normal grain growth in pure single phase systems, *Acta metall.,* **36,** 469–491.

Avrami, M., 1939. Kinetics of phase change. 1. General theory, *J. Chem. Phys.,* **7,** 1103–1112.

Avrami, M., 1940. Kinetics of phase change. II. Transformation-time relations for random distribution of nuclei, *J. Chem. Phys.,* **8,** 212–224.

Avrami, M., 1941. Kinetics of phase change. III. Granulations, phase change, and microstructure, *J. Chem. Phys.,* **9,** 177–184.

Axe, J.D. & Yamada, Y., 1986. Scaling relations for grain auto-correlation functions during nucleation and growth, *Phys. Rev. B,* **34,** 1599–1606.

Brandeis, G. & Jaupart, C., 1987. The kinetics of nucleation and crystal growth and scaling laws for magmatic crystallization, *Contrib. Mineral. Petrol.,* **96,** 24–34.

Brandeis, G., Jaupart, C. & Allègre, C.J., 1984. Nucleation, crystal growth and the thermal regime of cooling magmas, *J. geophys. Res. B,* **89,** 10 161–10 177.

Buyevich, Yu.A. & Mansurov, V.V., 1990. Kinetics of the intermediate stage of phase transition in batch crystallization, *J. Crystal Growth,* **104,** 861–867.

Cahn, J.W., 1956. The kinetics of grain boundary nucleated reactions, *Acta metall.*, **4**, 449–459.

Cashman, K.V. & Ferry, J.M., 1988. Crystal size distribution (CSD) in rocks and the kinetics and dynamics of crystallization. III. Metamorphic crystallization, *Contrib. Mineral. Petrol.*, **99**, 401–415.

Cashman, K.V. & Marsh, B.D., 1988. Crystal size distribution (CSD) in rocks and the kinetics and dynamic of crystallization. II. Makaopuhi lava lake, *Contrib. Mineral. Petrol.*, **99**, 292–305.

Christian, J.W., 1965. *The theory of transformations in metals and alloys*, Pergamon Press, New York, NY.

Cooper, R.F. & Kohlstedt, D.L., 1982. Interfacial energies in the olivine–basalt system, in *High Pressure Research in Geophysics*, pp. 217–228, eds Akimoto, S. & Manghnani, M.H., Reidel, Dordrecht.

Däßler, R. & Yuen, D.A., 1993. The effects of phase transition kinetics on subducting slabs, *Geophys. Res. Lett.*, **20**, 2603–2606.

Däßler, R., Yuen, D.A., Karato, S. & Riedel, M.R., 1993. Consequences of thermal-kinetic coupling on the phase boundaries of subducting slabs, *Research Report UMSI 93/152, Minnesota Supercomputer Institute.*

Dowty, E., 1980. Crystal growth and nucleation theory and the numerical simulation of igneous crystallization, in *Physics of Magmatic Processes*, pp. 419–485, ed. Hargraves, R.B., Princeton University Press, Princeton, NJ.

Fisher, M.E., 1967. The theory of condensation and the critical point, *Physics*, **3**, 255–283.

Frohlich, C., 1994. A break in the deep, *Nature*, **368**, 100–101.

Fujino, K. & Irifune, T., 1992. TEM studies on the olivine to modified spinel transformation in Mg_2SiO_4, in *High Pressure Research: Application to Earth and Planetary Sciences*, pp. 237–243, eds Syono, Y. & Manghnani, M.H., Terra Sci. Pub., Am. geophys. Un., Washington, DC.

Furu, T., Marthinsen, K. & Nes, E., 1990. Modelling recrystallization, *Mater. Sci. Technol.*, **6**, 1093–1102.

Gawlinski, E.T. & Stanley, H.E., 1981. Continuum percolation in two dimensions: Monte Carlo tests of scaling and universality of non-interacting discs, *J. Phys.* A: *Math. Gen.*, **14**, L291–L299.

Green, II, H.W. & Burnley, P.C., 1989. A new self-organizing mechanism for deep-focus earthquakes, *Nature*, **341**, 733–737.

Hamaya, N. & Akimoto, S., 1982. Experimental investigation on the mechanism of olivine → spinel transformation: growth of single crystal spinel from single crystal olivine in Ni_2SiO_4, in *High Pressure Research in Geophysics*, pp. 373–389, eds Akimoto, S. & Manghnani, M.H., Reidel, Dordrecht.

Hort, M. & Spohn, T., 1991. Numerical simulation of the crystallization of multicomponent melts in the thin dikes or sills 2. Effects of heterocatalytic nucleation and composition, *J. geophys. Res.* B, **96**, 485–499.

Johnson, W.A. & Mehl, R.F., 1939. Reaction kinetics in processes of nucleation and growth, *Trans. Am. Inst. Min. Metall. Engrs*, **135**, 416–458.

Karato, S., 1984. Grain-size distribution and rheology of the upper mantle, *Tectonophysics*, **104**, 155–176.

Katsura, T. & Ito, E., 1989. The system Mg_2SiO_4 – Fe_2SiO_4 at high pressures and temperatures: precise determination of stabilities of olivine, modified spinel and spinel, *J. geophys. Res.* B, **94**, 15 663–15 670.

Kirby, S.H., 1985. Rock mechanics observations pertinent to the rheology of the continental lithosphere and the localization of strain along shear zones, *Tectonophysics*, **119**, 1–27.

Kirby, S.H., 1987. Localized polymorphic phase transformations in high-pressure faults and applications to the physical mechanism of deep earthquakes, *J. geophys. Res.* B, **92**, 13 789–13 800.

Kirkpatrick, R.J., 1976. Towards a kinetic model for the crystallization of magma bodies, *J. geophys. Res.*, **81**, 2565–2571.

Kirkpatrick, R.J., 1981. Kinetics of crystallization of igneous rocks, in *Kinetics of Geochemical Processes*, pp. 321–398, eds Lasaga, A.C. & Kirkpatrick, R.J., Rev. Mineral., **8**, Mineral. Soc. Am., Chelsea, MI.

Kolmogorov, A.N., 1937. Statistical theory of nucleation processes, *Izv. Akad. Nauk SSSR, Ser. Math.*, **3**, 355–366.

Lofgren, G.E., 1983. Effect of heterogeneous nucleation on basaltic textures: A dynamic crystallization study, *J. Petrology*, **24**, 229–255.

Lorenz, B., Orgzall, I. & Heuer, H.-O., 1993. Universality and cluster structures in continuum models of percolation with two different radius distributions, *J. Phys.* A: *Math. Gen.*, **26**, 4711–4722.

McKenzie, D.P., 1969. Speculations on the consequences and causes of plate motions, *Geophys. J. R. astr. Soc.*, **18**, 1–32.

Mahin, K.W., Hanson, K. & Morris, J.W. Jr, 1980. Comparative analysis of the cellular and Johnson-Mehl microstructures through computer simulation, *Acta metall.*, **28**, 443–453.

Markworth, A.J., 1984. Analysis of the extent of growth-induced impingement for a simple model of precipitate nucleation and growth, *Scripta metall.*, **18**, 1309–1311.

Marsh, B.D., 1988. Crystal size distribution (CSD) in rocks and the kinetics and dynamics of crystallization 1. Theory, *Contrib. Mineral. Petrol.*, **99**, 277–291.

Meijering, J.L., 1953. Interface area, edge length, and number of vertices in crystal aggregates with random nucleation, *Philips Res. Rep.*, **8**, 270–290.

Morris, S., 1992. Stress relief during solid-state transformations in minerals, *Proc. R. Soc. Lond.* A, **436**, 203–216.

Orgzall, I. & Lorenz, B., 1988. Computer simulation of cluster-size distributions in nucleation and growth processes, *Acta metall.*, **36**, 627–631.

Pike, G.E. & Seager, C.H., 1974. Percolation and conductivity: A computer study. I., *Phys. Rev.* B, **10**, 1421–1434.

Randolph, A.D. & Larson, M.A., 1988. *Theory of Particulate Processes*, Academic Press, San Diego, CA.

Rubie, D.C., 1984. The olivine → spinel transformation and the rheology of subducting lithosphere, *Nature*, **308**, 505–508.

Rubie, D.C. & Ross II, C.R., 1994. Kinetics of the olivine–spinel transformation in subducting lithosphere: experimental constraints and implications for deep slab processes, *Phys. Earth planet. Inter.*, **86**, 223–241.

Rubie, D.C., Tsuchida, Y., Yagi, T., Utsumi, W., Kikegawa, T., Shimomura, O. & Brearley, A.J., 1990. An in situ x ray diffraction study of the kinetics of the Ni_2SiO_4 olivine–spinel transformation, *J. geophys. Res.* B, **95**, 15 829–15 844.

Ryum, N. & Hunderi, O., 1989. On the analytic description of normal grain growth, *Acta metall.*, **37**, 1375–1379.

Saetre, T.O., Hunderi, O. & Nes, E., 1986. Computer simulation of primary recrystallization microstructures: the effects of nucleation and growth kinetics, *Acta metall.*, **34**, 981–987.

Sekimoto, K., 1986. Evolution of the domain structure during the nucleation-and-growth process with non-conserved order parameter, *Physica* A, **135**, 328–346.

Solomatov, V.S. & Stevenson, D.J., 1993. Kinetics of crystal growth in a terrestrial magma ocean, *J. geophys. Res.* E, **98**, 5407–5418.

Spohn, T., Hort, M. & Fischer, H., 1988. Numerical simulation of the crystallization of multicomponent melts in thin dikes or sills. 1. The liquidus phase, *J. geophys. Res.* B, **93**, 4880–4894.

Stauffer, D., 1981. Scaling properties of percolation clusters, in *Lecture Notes in Physics*, **149**, pp. 9–25, eds Castellani, C., Di Castro, C. & Peliti, L., Springer-Verlag, Berlin.

Stauffer, D. & Aharony, A., 1992. *Introduction to Percolation Theory*, 2nd edn, Taylor & Francis, London.

Sung, C.M., 1979. Kinetics of the olivine–spinel transition under high pressure and temperature: experimental results and geophysical implications, in *High Pressure Science and Technology, vol. 2, Applications and Mechanical Properties*, pp. 31–42, eds Timmerhaus, K.D. & Barber, M.S., Plenum Press, New York, NY.

Thompson, A.H., 1991. Fractals in rock physics, *Ann. Rev. Earth planet. Sci.*, **19**, 237–262.

Tonks, W.B. & Melosh, H.J., 1990. The physics of crystal settling and suspension in a turbulent magma ocean, in *Origin of the Earth,*

pp. 151–171, eds Newsom, H.E. & Jones, J.H., Oxford University Press, New York, NY.

Turcotte, D.L. & Schubert, G., 1982. *Geodynamics. Applications of Continuum Physics to Geological Problems*, J. Wiley & Sons, New York, NY.

APPENDIX A: KINETIC EQUATION SET FOR NUCLEATION AND GROWTH

We give here a brief derivation of the equation set (5) for the droplet model of nucleation and growth.

Starting from the continuity equation (1) for the radial distribution function $n(r, t)$, the volume fraction of *untransformed* material is given in the thermodynamic limit by

$$\lim_{N\to\infty}\left(1-\frac{X_{3\text{-D}}}{N}\right)^N=\exp(-X_{3\text{-D}}) \tag{A1}$$

because of the statistical independence of different grains. The time development of $X_{3\text{-D}}$ is obtained by repeatedly performing partial integrations:

$$\begin{aligned}\frac{d}{dt}X_{3\text{-D}}(t)&=\int_0^\infty\frac{4\pi}{3}r^3\left[\frac{\partial}{\partial t}n(r,t)\right]dr\\&=\int_0^\infty\frac{4\pi}{3}r^3\left[-\frac{\partial}{\partial r}(Y(r,t)n(r,t))\right]dr\\&\simeq-\frac{4\pi}{3}Y(t)\int_0^\infty r^3\frac{\partial}{\partial r}n(r,t)\,dr\\&=4\pi Y(t)\int_0^\infty r^2n(r,t)\,dr-\frac{4\pi}{3}Y(t)[r^3n(r,t)]_{r=0}^{r=\infty}\\&=:4Y(t)X_{2\text{-D}}(t),\end{aligned}$$

where the last term in the square brackets vanishes because of the convergence of integral (6a). The third line is valid only approximately when the growth rate is not size-dependent, for example for an interface-controlled mechanism (Dowty 1980).

Eqs (5b) and (5c) are derived in complete analogy with

$$\begin{aligned}\frac{d}{dt}X_{2\text{-D}}(t)&=\int_0^\infty\pi r^2\left[\frac{\partial}{\partial t}n(r,t)\right]dr\\&=\int_0^\infty\pi r^2\left[-\frac{\partial}{\partial r}(Y(r,t)n(r,t))\right]dr\\&\simeq-\pi Y(t)\int_0^\infty r^2\frac{\partial}{\partial r}n(r,t)\,dr\\&=\pi Y(t)\int_0^\infty 2rn(r,t)\,dr-\pi Y(t)[r^2n(r,t)]_{r=0}^{r=\infty}\\&=:\pi Y(t)X_{1\text{-D}}(t)\end{aligned}$$

and

$$\begin{aligned}\frac{d}{dt}X_{1\text{-D}}(t)&=\int_0^\infty 2r\left[\frac{\partial}{\partial t}n(r,t)\right]dr\\&=\int_0^\infty 2r\left[-\frac{\partial}{\partial r}(Y(r,t)n(r,t))\right]dr\\&\simeq-2Y(t)\int_0^\infty r\frac{\partial}{\partial r}n(r,t)\,dr\\&=2Y(t)\int_0^\infty n(r,t)\,dr-2Y(t)[rn(r,t)]_{r=0}^{r=\infty}\\&=:2Y(t)X_{0\text{-D}}(t).\end{aligned}$$

Finally, eq. (5d) is obtained from the boundary condition (2b) according to

$$\begin{aligned}\frac{d}{dt}X_{0\text{-D}}(t)&=\int_0^\infty\frac{\partial}{\partial t}n(r,t)\,dr\\&=-[Y(r,t)n(r,t)]_{r=0}^{r=\infty}=Y(0,t)n(0,t)=:I^{\text{v}}(t).\end{aligned}$$